Icarus 309 (2018) 241–259

Contents lists available at ScienceDirect

Icarus

journal homepage: www.elsevier.com/locate/icarus

Spectroscopic examinations of hydro- and glaciovolcanic basaltic tuffs: Modes of alteration and relevance for Mars

W.H. Farrand[a,*], S.P. Wright[b], T.D. Glotch[c], C. Schröder[d], E.C. Sklute[e], M.D. Dyar[e]

[a] Space Science Institute, 4750 Walnut Street, Suite 205, Boulder, CO 80301, USA
[b] Planetary Science Institute, 1700 East Ft. Lowell, Suite 106, Tucson, AZ 85719, USA
[c] Department of Geosciences, Stony Brook University, 255 Earth and Space Sciences Building, Stony Brook, NY 11794, USA
[d] Department of Biological and Environmental Sciences, University of Stirling, FK9 4LA Scotland, UK
[e] Department of Astronomy, Mount Holyoke College, 206 Kendade, South Hadley, MA 01075, USA

ARTICLE INFO

Article history:
Received 14 July 2017
Revised 22 December 2017
Accepted 8 March 2018
Available online 10 March 2018

Keywords:
Mars, surface
Mineralogy
Volcanism
Earth
Spectroscopy

ABSTRACT

Hydro- and glaciovolcanism are processes that have taken place on both Earth and Mars. The amount of materials produced by these processes that are present in the martian surface layer is unknown, but may be substantial. We have used Mars rover analogue analysis techniques to examine altered tuff samples collected from multiple hydrovolcanic features, tuff rings and tuff cones, in the American west and from glaciovolcanic hyaloclastite ridges in Washington state and in Iceland. Analysis methods include VNIR-SWIR reflectance, MWIR thermal emissivity, thin section petrography, XRD, XRF, and Mössbauer spectroscopy. We distinguish three main types of tuff that differ prominently in petrography and VNIR-SWIR reflectance: minimally altered sideromelane tuff, gray to brown colored smectite-bearing tuff, and highly palagonitized tuff. Differences are also observed between the tuffs associated with hydrovolcanic tuff rings and tuff cones and those forming glaciovolcanic hyaloclastite ridges. For the locations sampled, hydrovolcanic palagonite tuffs are more smectite and zeolite rich while the palagonitized hyaloclastites from the sampled glaciovolcanic sites are largely devoid of zeolites and relatively lacking in smectites as well. The gray to brown colored tuffs are only observed in the hydrovolcanic deposits and appear to represent a distinct alteration pathway, with formation of smectites without associated palagonite formation. This is attributed to lower temperatures and possibly longer time scale alteration. Altered hydro- or glaciovolcanic materials might be recognized on the surface of Mars with rover-based instrumentation based on the results of this study.

1. Introduction

The surface of Mars is primarily basaltic in composition and has been formed and modified through volcanic and impact processes as well as aqueous alteration early in its geologic history. The Mars Science Laboratory (MSL) rover Curiosity, through its CheMin X-Ray Diffraction (XRD) instrument has found a ubiquitous X-ray amorphous component (e.g., Bish et al., 2013; Downs et al., 2015). While this amorphous component almost certainly contains poorly crystalline minerals, glass is also a likely constituent. Glass has also been modeled as a major constituent of rocks observed by the Mars Exploration Rover (MER) Spirit in the Columbia Hills of Gusev crater (Ruff et al., 2006, 2008) and has been hypothesized as being a major constituent in the northern plains (Bandfield et al., 2000; Horgan and Bell, 2012). Basaltic glass results from the rapid cooling of basaltic lava in eruptive processes such as fire fountaining, in explosive hydrovolcanic eruptions, or from the rapid cooling of impact melt. Glass is a metastable material and will alter through interactions with the surrounding environment over time. However, in the martian surface environment of frigid temperatures, and a relative lack of chemical weathering agents (e.g., liquid water), glass could persist much longer than it can in the terrestrial surface environment. Nevertheless, as glass alters, the form of that alteration, and the secondary minerals that are produced, provide a record of the environmental conditions extant at the time of alteration. Thus, assessing the types of alteration products in the martian geologic record can provide information on the causative environments that produced them.

In this study, we have analyzed several relatively fresh and altered basaltic tephras from hydrovolcanic edifices in the western United States and a limited set of glaciovolcanic hyaloclastites from the Pacific Northwest and Iceland in order to assess modes of alteration. This paper addresses the alteration products of hydro-

* Corresponding author.
E-mail address: farrand@spacescience.org (W.H. Farrand).

https://doi.org/10.1016/j.icarus.2018.03.005
0019-1035/

and glaciovolcanic tephras and is a companion paper to Farrand et al. (2016), which was primarily concerned with characteristics of minimally altered basaltic glass formed in the same environments as well as impact melt glasses. Fisher and Schmincke (1984) described the broad category of "volcaniclastic" rocks as consisting of "all clastic volcanic materials formed by any process of fragmentation, dispersed by any kind of transporting agent, deposited in any environment or mixed in any significant portion with nonvolcanic fragments" with this term being generally synonymous with "tephra". Fisher and Schmincke (1984) described the category of "hydroclastic" material as consisting of "pyroclasts formed from steam explosions at magma-water interfaces". Thus, in the present work we are primarily concerned with this subset of hydroclastic materials. Also, the sampled materials were all indurated, to varying extents, and thus can be described as "hydroclastic tuffs" which are essentially the same as "hyaloclastites" (although as used in the literature, the former might have more of a uniformly fine-grained composition while the latter can be more of a breccia). Fresh hydroclastic tuffs consist of basaltic glass (sideromelane), partially devitrified basaltic glass (tachylite), and varying fractions of crystalline minerals associated with basalts (olivine, pyroxene, plagioclase, and oxides such as ilmenite and/or magnetite).

Glasses produced by hydro- and glaciovolcanic activity alter into the poorly crystalline material palagonite (Stroncik and Schmincke, 2002) and ultimately into crystalline products—primarily smectites and zeolites. Palagonitization of hydro- and glaciovolcanic glasses is controlled by several factors including the action of heated water (e.g., Jakobsson and Moore, 1986; Schiffman et al., 2000; Bishop et al., 2002) and, as noted by Pauly et al. (2011), another important control on the extent of palagonitization is the porosity (which dictates the water/rock ratio).

Schiffman et al. (2000, 2002) described a pathway of alteration under ambient temperature conditions for glassy basaltic ash that they described as "pedogenic" alteration. Under this alteration pathway, the alteration products are largely disaggregated and included, under annual rainfall conditions of less than 50 cm/year, minor smectite, and, with higher rainfall of more than 250 cm/year, mainly kaolinite, allophane, and/or imogolite. This is in contrast to the palagonitic alteration of basaltic glass that results in the formation of rinds of palagonite on glass grains, and cementation of the ash through the development of smectite (Schiffman et al., 2002 indicated the smectite in the palagonitized materials to be either a di-octahedral smectite such as a nontronite or a tri-octahedral smectite such as a saponite) and zeolites (primarily chabazite and phillipsite). Researchers examining pedogenically altered disaggregated tephras in locations such as the summit of Mauna Kea have referred to those products as "palagonites" (e.g., Evans and Adams, 1980, Allen et al., 1981; Morris et al., 1990) although, as noted by Schiffman et al. (2000, 2002), they are not cemented, have not been subjected to hydrothermal alteration, and differ in mineralogy from hydrothermally altered palagonite tuffs.

In general, palagonitic alteration requires elevated temperatures. Jakobsson and Moore (1986), in examining the palagonitization of Surtsey tephras in temperature regimes up to 100 °C, noted the temperature dependence on the rate and extent of palagonitization saying that the rate of palagonitization doubled with every 12 °C increase in temperature. In many hydrovolcanic vents, such as tuff cones, the palagonite tuffs are mantled by gray tuffs largely lacking in palagonite. Jakobsson and Gudmundsson (2008), in discussing Icelandic tuyas and hyaloclastite ridges and mounds, refer to these as "outer slope hyaloclastites" and distinguished them from hydrothermally formed palagonitized hyaloclastites. Wohletz and Sheridan (1983) accounted for the extensive palagonitization of tuff cones such as Pavant Butte in Utah and Cerro Colorado in Sonora, Mexico as the result of the deposition of steam with the ash, a consequence of the abundant water supply associated with tuff cone formation. The gray mantling tuffs, as in Fig. 1A, represent a blanketing layer allowing for the retention of heat and the promotion of palagonitization. These gray tuffs are either ashes emplaced in the same manner as the massively bedded palagonite tuffs below, but which cooled too rapidly to palagonitize (as with the sideromelane tuffs of Fig. 1B), or late stage surge beds as described by Wohletz and Sheridan (1983) for locations such as the Cerro Colorado tuff cone of Sonora, Mexico. Massively bedded tuffs that are gray to brown in color also occur within sequences of beds overlying or underlying palagonite tuffs (Fig. 1C and D). These gray to brown unpalagonitized to poorly palagonitized tuffs are one of the main foci of this paper since they have generally been ignored in the literature regarding alteration products associated with hydro- and glaciovolcanism. These tuffs are distinct in terms of composition, spectral reflectance (Farrand and Singer, 1992), and petrography from palagonite tuffs (Fig. 1B–D) and the minimally altered sideromelane tuffs (Fig. 1B) described more thoroughly in Farrand et al. (2016).

These three types of tuffs (sideromelane tuffs, gray to brown tuffs, and palagonite tuffs) nominally correspond to the three zones of alteration observed by Walton and Schiffman (2003) who examined a drill core containing altered volcanic products from Mauna Kea. Those authors found three distinct zones of alteration of the sideromelane which from highest to lowest were: (1) a zone of incipient alteration, (2) a zone of smectitic alteration, and (3) a zone of palagonitic alteration. In the first, they found fractured glass grains and smectite beginning to form as a coating in pores and on grains. In the deeper zone of smectitic alteration, they found additional growth of pore-lining smectite as well as the development of a pore-filling and grain-replacing smectite (nominally saponite) along with the development of the zeolite mineral phillipsite. In the deepest zone of palagonitic alteration, the sideromelane was partially replaced by palagonite and there was also the development of the pore-filling zeolite mineral chabazite. Walton and Schiffman (2003) described the smectitic and palagonitic modes of alteration as being divergent from palagonite formation after the formation of the smectites. This type of alteration of glass to smectite without the intermediate development of palagonite rinds was also described by Jeong and Sohn (2011) for altered hyaloclastites from Jeju Island, Korea. The observed smectitic alteration is in contrast to previous studies (e.g., Stroncik and Schmincke, 2002), which have described palagonite as an intermediate product between basaltic glass and smectites. In the palagonitic alteration mode, palagonite *is* an intermediate product; however, in the alternate smectitic mode of alteration, smectite forms without evidence of extensive palagonite rind development. Examples of this type of alteration from the field areas examined in this study will be presented in this paper.

In order to examine the alteration products of basaltic glass associated with hydro- and glaciovolcanic vents, we have examined tuffs from a number of tuff rings, tuff cones, and a pair of subglacially formed hyaloclastite ridges (aka, tindars; Smellie and Edwards, 2016). The tuff samples collected from the field sites have been examined using Mars rover analogue measurement approaches which include visible / near infrared (VNIR) to shortwave infrared (SWIR) to mid-wave infrared (MWIR) reflectance spectroscopy; MWIR thermal emission spectroscopy; X-ray diffraction (XRD) analysis; X-ray fluorescence (XRF) for major and minor element chemistry; and Mössbauer spectroscopy of some samples. A number of samples have also been examined with laboratory techniques including thin section petrography, loss on ignition, and FeO titration.

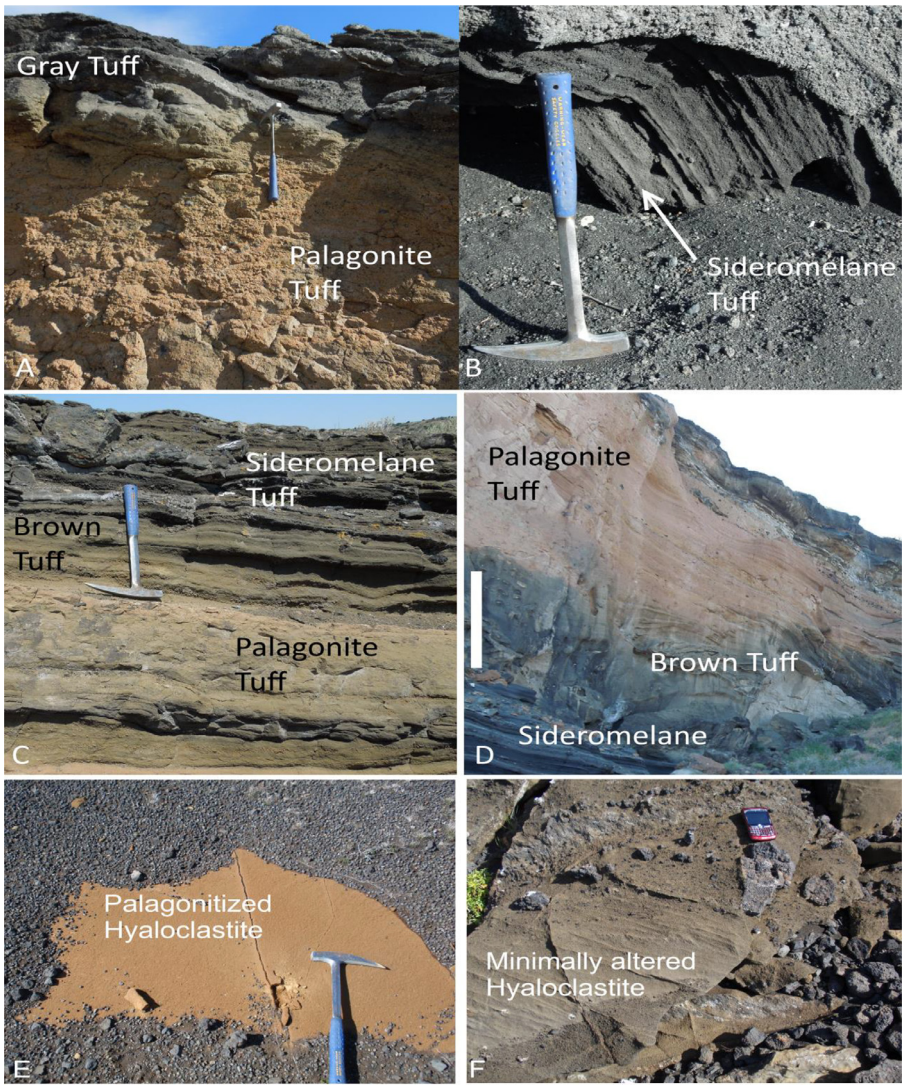

Fig. 1. (A) Gray mantling tuffs overlying orange palagonite tuffs at Pavant Butte. Sampling site for samples PB13-04A, B, and C (sideromelane, gray mantling, and palagonite tuffs). Rock hammer for scale. (B) Thinly bedded sideromelane tuffs at Pavant Butte, Utah. Rock hammer for scale. (C) Brown tuff overlying palagonite tuff at N. Menan Butte. Sampling site for samples NMB12-08 (brown tuff) and NMB12-07 (palagonite tuff). Rock hammer for scale. (D) Basal thinly bedded sideromelane overlain by massively bedded brown and palagonite tuff at Pavant Butte. White scale bar is ~1.5 m in length. (E) Palagonitized hyaloclastite at Helgafell. Sampling site for Hf-02. Rock hammer for scale. (F) Minimally altered sideromelane hyaloclastite at Helgafell. Sampling site for Hf-06. Blackberry mobile phone (12 cm in length) for scale. (For interpretation of the references to color in this figure legend, the reader is referred to the web version of this article.)

2. Sample suite

Field work was conducted for this research at sites in Idaho, New Mexico, and Utah listed in Table 1. Tuff cones sampled in Idaho included N. Menan Butte (Creighton, 1987), Sinker Butte (Brand and White, 2007), and White Butte (Godchaux et al., 1992). Sinker Butte is an emergent tuff cone that was formed in and above Pleistocene-aged Lake Idaho. N. Menan Butte is one of the two Menan Buttes formed, according to Creighton (1987), as a result of eruption through a healthy aquifer system. According to Godchaux et al. (1992), White Butte was erupted entirely subaqueously. Also sampled was the Split Butte tuff ring in Craters of the Moon National Monument, which was formed in a phreatomagmatic eruption (Womer, 1977). In New Mexico, the Zuni Salt Lake (Crumpler and Aubele, 2001) and Narbona Pass Maar (Brand et al., 2009), which were both formed in phreatomagmatic eruptions, were sampled. In Utah, the Pavant Butte tuff cone (alternatively spelled "Pahvant Butte" on some maps) was sampled. Pavant Butte is an emergent tuff cone erupted into Pleistocene-aged Lake Bonneville (Wohletz and Sheridan, 1983; Farrand and Singer, 1991; White, 1996). The Zuni Salt Lake and Narbona Pass Maar sites had high fractions of country rock and crystalline fragments; thus, since the focus of this paper focuses on the alteration of basaltic glass, we only make use of a subset of Zuni Salt Lake samples that were more glass-rich.

Other samples, collected from previous projects, were also examined in this work, but sampling from these sites was not as extensive or as well documented. These included glaciovolcanic hyaloclastites from the Crazy Hills hyaloclastites ridges in the Indian Heaven Volcanic Field of southern Washington (Hammond, 1987; Farrand and Lane, 2002) and the Helgafell hyaloclastite ridge (Schopka et al., 2006) in Iceland.

3. Measurements and analysis approaches

The analysis approach of this research was to make use of analysis techniques that can be conducted by current or planned Mars rovers where possible, but to supplement these with laboratory techniques (petrography of thin sections, micro-FTIR analyses) where these could further inform our understanding of the sam-

Table 1
Hydro- and glaciovolcanic features sampled for this paper, their geographic coordinates, types, and approximate ages.

Location	Latitude	Longitude	Type	Approx. age
Sinker Butte	43.23°N	116.39°W	Emergent Tuff Cone	Between 1.25 ± 0.2 and 1.17 ± 0.2 Ma[a]
N. Menan Butte	43.79°N	111.97°W	Subaerial Tuff Cone	Mid to Late Pleistocene[b] (~0.78–0.015 Ma)
Split Butte	42.90°N	113.37°W	Tuff Ring	>2130 years BP[c]
Pavant Butte	39.13°N	112.55°W	Emergent Tuff Cone	15,300 years BP[d]
White Butte	43.33°N	116.56°W	Subaqueous Tuff Cone	Pliocene – Pleistocene[e]
Zuni Salt Lake	34.45°N	108.77°W	Tuff Ring	0.086 ± 0.03 Ma[f]
Crazy Hills	46.05°N	121.86°W	Hyaloclastite Ridges	130,000 to 190,000 years BP[g]
Helgafell	64.01°N	21.85°W	Hyaloclastite Ridge	Weichselian[h]

[a] Brand and White (2007).
[b] Creighton (1987).
[c] Womer (1977).
[d] Oviatt and Nash (1989).
[e] Godchaux et al. (1992).
[f] McIntosh and Chamberlin (1994).
[g] Hammond (1987).
[h] Schopka et al. (2006).

ples being analyzed. Given constraints in available resources and the fact that samples were acquired over the course of two years for the hydrovolcanic-focused part of this investigation and with some samples coming from previous limited field work, samples were analyzed as resources and measurement capabilities became available with the consequence that there was not a comprehensive set of all measurements applied to all samples. Samples analyzed and measurements made are summarized in Table 2.

3.1. VNIR, SWIR, and MWIR reflectance spectroscopy

An initial assessment of surface materials encountered by a Mars rover can be in the form of multispectral VNIR imagery (e.g., the MER Pancam, MSL Mastcam, or the planned ExoMars PanCam or Mars 2020 Mastcam-Z) or, for the planned ExoMars rover, a hyperspectral micro-image of a surface (as will be collected at the micro-scale by the MicrOmega infrared spectrometer Leroi et al., 2009). Additionally, point spectra in the NIR spectral range will be collected with the ExoMars ISEM instrument (Korablev et al., 2014) or the NIR spectrometer component of the Mars 2020 SuperCam (Wiens et al., 2016). With the goal of characterizing such materials in this fashion, preliminary spectra of most of the field samples were collected with the University of Colorado CIRES ASD FieldSpec reflectance spectrometer. A subset of samples were ground with a stainless steel mortar and pestle and filtered through a 400 µm mesh and their bi-directional reflectance spectra were measured over the range of 0.3–2.6 µm at the Brown University RELAB facility. Procedures for collecting bi-directional reflectance at RELAB were described by Pieters (1983) and Pieters et al. (1996). Briefly, bi-directional reflectance measurements were made under room temperature and ambient (generally 40% humidity) laboratory conditions on RELAB's UV–Vis-NIR Bidirectional Spectrometer. Measurements were made using a pressed halon standard and corrected using a calibration table made based on National Bureau of Standard data and corrected for minor non-Lambertian behavior by measuring RELAB halon against diffuse gold and sulfur powder over the 2–2.6 µm range using an incidence angle of 30° and emission angle of 0°. The same subset of samples was also measured with the RELAB Nicolet 740 FT-IR spectrometer collecting biconical reflectance from 0.83 to 25 µm in a dry-air purged environment relative to a diffuse gold standard. Additional details on measurement procedures are available in the RELAB User's Manual (http://www.planetary.brown.edu/relabdocs/RelabManual2006a.pdf). We also note that the reflectance spectra discussed here are now available on the RELAB web site (http://www.planetary.brown.edu/relab/).

3.2. TIR thermal emission spectroscopy

Thermal emission spectra of unprocessed hand samples were collected using similarly configured instruments at Arizona State University, Stony Brook University, and at the Southwest Research Institute (SWRI) in Boulder (using, respectively, Nicolet Nexus 670, Nicolet 6700, and Nicolet 470 spectrometers). The systems used, and sample measurement procedures followed, are those described in Ruff et al. (1997). However, in brief, samples were heated in an oven and kept at approximately 80 °C during spectral acquisition. The radiance of each sample was collected over 270 scans that were averaged to produce one spectrum. The sample temperature was kept between that of the two blackbodies which were at 70 °C and 100 °C. The spectra collected at SWRI and Stony Brook were resampled to match the 923 channel wavenumber set of the ASU spectrometer covering the spectral range of 2000–220 cm^{-1} (5–45 µm). These spectra were subjected to analysis using the linear deconvolution methodology first described by Ramsey and Christensen (1998) and modified by Rogers and Aharonson (2008). A spectral library based on that used by Hamilton et al. (2008) was used for the linear deconvolution analysis using MATLAB software implementing the Rogers and Aharonson (2008) approach. Results are described in Section 4.3 below.

3.3. Thin section petrography and Micro-FTIR analysis

Thin sections were made of samples noted in Table 2. Photomicrographs were collected in plane polarized and cross polarized light and point counts were made using the JMicroVision software. Approximately 400 points were collected per image with two to four images examined per thin section.

Uncovered thin sections were examined at the Stony Brook University Vibrational Spectroscopy Laboratory using a Nicolet iN10MX FTIR microscope with a liquid nitrogen cooled 16 pixel Hg-Cd-Te linear array detector. This instrument was used to collect hyperspectral image cubes (in reflectance) of portions of the thin sections noted in Table 2 between 4000 and 715 cm^{-1}. (2.5–14 µm). Select point spectra were also collected over the broader range of 4000–400 cm^{-1}. (2.5–25 µm). The spatial resolution of the instrument is 25 µm/pixel. These hyperspectral image cubes were analyzed using an iterative linear spectral mixture analysis (SMA) methodology (Adams et al., 1993). Three to four endmembers were selected by inspection (for example, glass, zeolites, and palagonite rinds), were subjected to SMA and the resulting RMS error image was examined with additional endmembers selected from coherent regions with high RMS error. We then ran the SMA routine again with the addition of the new endmembers and the

Table 2
Samples reported on in this paper, the hydro- or glaciovolcanic feature from which they were collected, their type, environment of deposition, and the analysis techniques to which each was subjected.

Sample	From	Type	Environment of deposition	Thin Section	Micro-FTIR	Reflectance	Emissivity	XRF	XRD	MB
NMB12-01	N. Menan Butte	Sideromelane Tuff	Subaerial	X	X	X	X	X	X	
NMB12-02	N. Menan Butte	Sideromelane Tuff	Subaerial			X	X			
NMB12-03	N. Menan Butte	Palagonite Tuff	Subaerial	X	X	X	X	X		
NMB12-04	N. Menan Butte	Palagonite Tuff	Subaerial	X		X	X	X	X	X
NMB12-05	N. Menan Butte	Gray/Brown Tuff	Subaerial			X	X	X	X	X
NMB12-06	N. Menan Butte	Sideromelane Tuff	Subaerial			X	X	X	X	
NMB12-07	N. Menan Butte	Palagonite Tuff	Subaerial	X	X	X	X	X	X	X
NMB12-08	N. Menan Butte	Gray/Brown Tuff	Subaerial							X
NMB12-09	N. Menan Butte	Sideromelane Tuff	Subaerial	X	X	X	X	X	X	
NMB12-12	N. Menan Butte	Gray/Brown Tuff	Subaerial	X		X	X		X	
NMB12-14	N. Menan Butte	Sideromelane Tuff	Subaerial	X	X	X	X	X	X	
SB12-07	Sinker Butte	Palagonite Tuff	Subaerial	X		X	X	X		X
SB12-21	Sinker Butte	Palagonite Tuff	Subaerial			X	X	X	X	X
SB12N-03	Sinker Butte	Palagonite Tuff	Subaerial	X	X	X	X	X	X	
SB12N-04	Sinker Butte	Gray/Brown Tuff	Subaerial	X		X	X	X	X	
SB12S-01	Sinker Butte	Palagonite Tuff	Subaerial	X		X	X	X	X	X
SplB12-06	Split Butte	Palagonite Tuff	Subaerial	X	X	X	X	X	X	
SplB12-08	Split Butte	Palagonite Tuff	Subaerial	X	X	X	X	X	X	
SplB12-09	Split Butte	Palagonite Tuff	Subaerial	X	X	X	X		X	
PB13-04A	Pavant Butte	Sideromelane Tuff	Subaerial	X	X	X	X	X	X	
PB13-04B	Pavant Butte	Gray/Brown Tuff	Subaerial	X	X	X	X	X	X	X
PB13-04C	Pavant Butte	Palagonite Tuff	Subaerial	X	X	X	X	X	X	
PB13-05A	Pavant Butte	Palagonite Tuff	Subaerial			X	X	X	X	X
PB13-05B	Pavant Butte	Gray/Brown Tuff	Subaerial	X	X	X	X		X	X
PB13-08	Pavant Butte	Gray/Brown Tuff	Subaerial	X	X	X	X		X	X
PB13-11	Pavant Butte	Sideromelane Tuff	Possibly Subaqueous			X	X	X		
PB13-13	Pavant Butte	Palagonite Tuff	Subaerial	X	X	X	X	X	X	X
PB13-14	Pavant Butte	Palagonite Tuff	Subaerial	X	X	X	X	X	X	
WhB12-01	White Butte	Gray/Brown Tuff	Subaqueous			X				
WhB12-03	White Butte	Palagonite Tuff	Subaqueous	X		X	X	X	X	
WhB12-04	White Butte	Gray/Brown Tuff	Subaqueous	X		X	X			
WhB12-05	White Butte	Sideromelane Tuff	Subaqueous			X	X	X		
ZSL13-05	Zuni Salt Lake	Gray/Brown Tuff	Subaerial		X	X	X	X	X	
ZSL13-08	Zuni Salt Lake	Gray/Brown Tuff	Subaerial		X	X	X	X	X	
CH-02	Crazy Hills	Sideromelane Tuff	Subglacial	X		X	X	X		
CH-04	Crazy Hills	Palagonitized Hyaloclastite	Subglacial	X		X	X	X		
CH-10	Crazy Hills	Palagonitized Hyaloclastite	Subglacial			X	X	X		
Hf-01	Helgafell	Partially Palagonitized Hyaloclastite	Subglacial	X		X	X	X		
Hf-02	Helgafell	Partially Palagonitized Hyaloclastite	Subglacial	X		X	X	X		X
Hf-03	Helgafell	Partially Palagonitized Hyaloclastite	Subglacial			X	X	X		X
Hf-04	Helgafell	Partially Palagonitized Hyaloclastite	Subglacial	X		X	X			X
Hf-06	Helgafell	Minimally Altered Hyaloclastite	Subglacial	X		X	X			X
Hf-07	Helgafell	Minimally Altered Hyaloclastite	Subglacial			X	X	X		

Table 3
Samples with positive XRD identifications of alteration minerals.

Sample	Alteration phase(s)	Mineral group(s)	Peaks identified (° 2θ)
SB12N-03	Phillipsite	Zeolite	27.9, 12.3
SB12S-01	Nontronite	Smectite	5.7, 60.9
SB12-21	Chabazite, Nontronite	Zeolite, Smectite	30.4, 20.4, 9.4; 5.7, 19.4
SplB12-06A	Phillipsite	Zeolite	27.9, 12.3
PB13-04C	Chabazite-K, Calcite	Zeolite, Carbonate	30.3, 20.5, 9.4; 29.5
WhB12-03	Chabazite-Ca, Calcite	Zeolite, Carbonate	30.4, 20.5, 9.4; 29.5, 47.6

resulting RMS error image examined again for potential additional endmember(s). This process was repeated until a bland, essentially featureless RMS error image resulted from the SMA. Classification maps of the Micro-FTIR image cubes were then made using the spectral angle mapper (SAM) (Kruse et al., 1993) and spectral information divergence (SID) (Chang, 2000) classification programs.

3.4. XRF major and minor element chemistry

XRF measurements of relatively unaltered as well as altered hydro- and glaciovolcanic glasses, listed in Table 2, were made by Dr. S. A. Mertzman of Franklin & Marshall College on a PANalytical 2404R X-ray fluorescence vacuum spectrometer equipped with a 4 kW Rh super sharp X-ray tube. Samples were ground in ceramic grinding vessels to a finer than 80 mesh particle size. 0.4000 g of anhydrous whole rock powder was mixed with 3.6000 g of Li2B4O7 flux and fused into homogeneous glass disks for major element chemistry. 7.0000 g of whole rock powder was mixed with a Copolywax binder and pressed under 50,000 psi to form briquettes for trace element analysis including Rb, Sr, Y, Zr, Nb, Ni, Ga, Cu, Zn, U, Th, Co, Pb, Sc, Cr, V, La, Ce, and Ba at the ppm level. Each element was measured under somewhat different setting of kV and mA ranging for 60 kV and 66 mA for higher atomic numbered elements to 24 kV and 125 mA for the low atomic numbered elements. Also determined were loss-on-ignition (LOI) by heating a known amount of sample in a furnace at 950 °C for 1.5 h. The %FeO was measured via a titration technique and the amount of Fe_2O_3

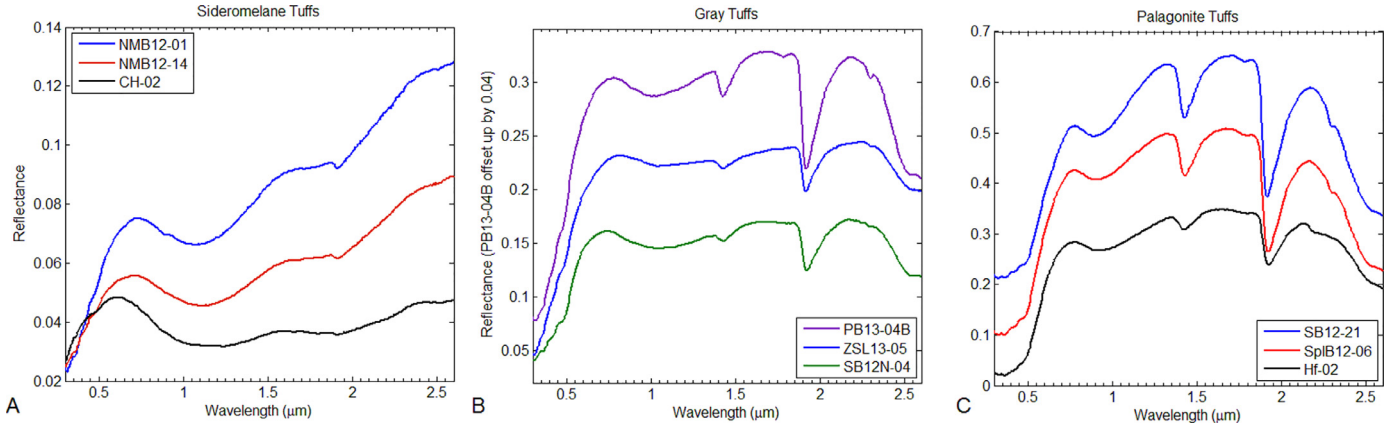

Fig. 2. (A) Glass-rich, sideromelane tuffs from N. Menan Butte (NMB) and Crazy Hills (CH). (B) Gray tuffs with intermediate levels of alteration from Pavant Butte (PB), Zuni Salt Lake (ZSL), and Sinker Butte (SB). (C) Highly palagonitized tuffs from Sinker Butte (SB), Split Butte (SplB), and Helgafell (Hf).

was calculated given the total amount of iron in the sample that was determined by XRF.

3.5. X-Ray diffraction

XRD analysis was performed on a number of powdered samples using the Auburn University Bruker X-Ray Diffractometer using Cu-Kα radiation. XRD patterns were analyzed using the Match! software of Crystal Impact GmbH. XRD is challenging on these samples given their generally poorly crystalline nature; however, for some of the more highly altered samples, alteration phases were detected as described below in Section 4.4.

3.6. Mössbauer spectroscopy

Mössbauer spectroscopy was performed on a subset of samples (Table 2) using either a miniaturized Mössbauer spectrometers MIMOS II (Klingelhöfer et al., 1996; Klingelhöfer et al., 2003) at the University of Stirling in the UK, or at Mt. Holyoke University using a SEE Co. W100 spectrometer.

The University of Stirling analyses were performed using ^{57}Co in Rh matrix as a γ-radiation source at constant acceleration (triangular waveform). Measurements were performed at room temperature and calibrated against a spectrum of α-Fe(0). Spectra obtained with MIMOS II were fitted with an in-house routine, Mbfit, based on the least squares minimization routine MINUIT (James, 2004) using Lorentzian lineshapes. No f-factor correction was applied

The Mt. Holyoke analyses were conducted using a ~55 mCi 57Co source in rhodium. Spectra were calibrated to α-Fe foil and run times were typically 24–48 h. Mössbauer data were fit using Mexfieldd, a program provided by E. DeGrave at the University of Ghent, Belgium. The program solves the full hyperfine interaction Hamiltonian to fit Lorentzian doublets to the spectral data with isomer shift (δ), quadrupole splitting (Δ), and full width at half maximum (Γ) as free parameters (Degrave and Vanalboom, 1991; Vandenbergh et al., 1994). Mössbauer parameters from measurements are listed in Supplementary Table 1.

4. Results

4.1. VNIR, SWIR, and MWIR reflectance spectroscopy

4.1.1. VNIR–SWIR reflectance

As was noted above, we distinguish three main types of tuff associated with the hydro- and glaciovolcanic vents that were sampled: black to gray sideromelane tuff, gray to brown tuffs, and highly indurated palagonite tuff. Representative bi-directional reflectance spectra of these three main types of tuff are shown in Fig. 2. Combined VNIR-MWIR reflectance spectra of all spectra cited in Table 2 are provided in supplementary Table 2.

The sideromelane tuffs are characterized by a black to gray color. The darkest tuffs are characterized primarily by broad Fe^{2+} in glass crystal field bands centered from 1.05 to 1.15 μm and near 1.97 μm as noted by Farrand et al. (2016) with supplementary detail on the reflectance of basaltic glasses in Adams (1975), Cloutis et al. (1990), Farrand and Singer (1992), Minitti et al. (2002) and Horgan et al. (2014). With increasing albedo, they exhibit an increasingly distinct red slope from 0.75 to 2.6 μm. Also with increasing albedo they display a stronger 1.9 μm band. The gray to brown tuffs have a flat slope from 0.75 to 2.1 μm, 1.4 and 1.9 μm water overtone bands of varying strength, a drop in reflectance longwards of 2.35 μm, and have a band at 2.29 μm that we attribute to a combination Fe–OH bend plus OH stretch (Fig. 3), nominally attributable to nontronite. The palagonite tuffs are orange to brown in color, have broadly convex continua shapes from 0.78 to 2.6 μm, have deep 1.4 and 1.9 μm water overtone bands, can have both 2.2 and 2.29 μm bands or potentially, just the 2.29 or just the 2.2 μm band, and can have a band centered near 2.5 μm (Fig. 3).

We note spectral differences between the palagonite tuffs formed at the hydrovolcanic centers and palagonitized hyaloclastite from the sampled glaciovolcanic hyaloclastite ridges. The latter display only the 2.2 μm band (Fig. 4; no 2.29 μm band) and have only a weak 2.5 μm band. Fig. 4B and C show library spectra of poorly-ordered Al phyllosilicates imogolite and allophane which have band centers at a shorter wavelength than that of the well-ordered Al-smectite montmorillonite. Bishop et al. (2002), in their study of a palagonitized hyaloclastite from Thórólfsfell in Iceland, noted that poorly-ordered Al phyllosilicates, such as imogolite and allophane, were likely present. Other researchers have described gel-palagonite as having the chemical composition of an Fe-rich montmorillonite (Drief and Schiffman, 2004) which could account for the predominance of a 2.2 μm band in samples with mostly gel palagonite without fibro-palagonite or pore-filling smectite development. Hydrovolcanic palagonite tuffs have a 2.29 μm feature that is stronger than any 2.2 μm band that might be present (Fig. 3) due to the growth of smectites that are nominally more nontronitic. The hydrovolcanic palagonite tuffs also display a stronger band in the 2.5 μm region.

4.1.2. MWIR reflectance

Reflectance features in the 3–6.5 μm range of basaltic tephras in various stages of alteration have not, to our knowledge, been

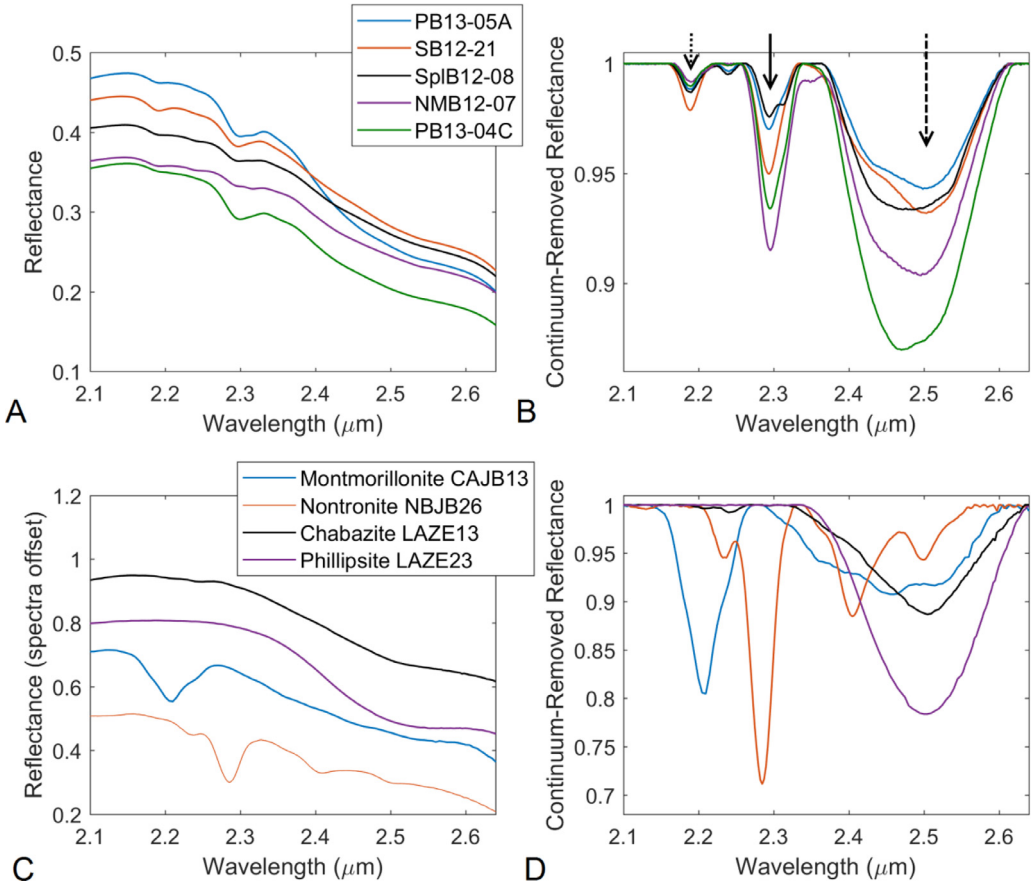

Fig. 3. (A) Reflectance in the 2.1 to 2.64 μm region of hydrovolcanic palagonite tuffs from Pavant Butte (PB), Sinker Butte (SB), North Menan Butte (NMB) and Split Butte (SplB). (B) Continuum-removed versions of these spectra. Dotted arrow indicates 2.2 μm band, solid arrow indicates 2.29 μm band, and dashed arrow indicates 2.5 μm band. (C) Laboratory spectra of clay (montmorillonite and nontronite) and zeolite (chabazite and phillipsite) minerals associated with palagonite tuffs. (D) Continuum-removed versions of these clay and zeolite sample spectra.

previously described. As noted in our companion paper (Farrand et al., 2016) that deals more extensively with minimally altered sideromelane tuffs, there is a Si–O overtone band in such samples at 5.32 μm. This feature weakens as the starting sideromelane alters to other phases.

The depth of 3 and 6 μm H_2O bands increases with increasing alteration and associated hydration. For palagonite tuffs associated with hydrovolcanic tuff rings and tuff cones, a band centered at, or near, 4.5 μm is present (Fig. 5A) which we attribute to the presence of zeolite minerals. Cloutis et al. (2002) note this band in zeolite spectra and they attribute it to the first overtone of the main SiO_4 stretching vibration, in their "group 4" zeolites which consist principally of chabazite. Chabazite is a zeolite mineral that is often noted as occurring in the alteration products of basaltic tuffs (e.g., Stroncik and Schmincke, 2001). This 4.5 μm band is not present in glaciovolcanic palagonitized hyaloclastites (Fig. 5B). The reasons for the differences between these two classes of materials are addressed in the *Discussion* section below.

An asymmetric narrow band is observed in some of the tuff ring and tuff cone palagonite tuff spectra at 3.98 μm which we attribute to carbonate in the samples. As discussed in Section 4.2 below, minor amounts of carbonate are also observed in the micro-FTIR hyperspectral image cubes and also in the bulk sample emissivity spectra discussed in Section 4.3. Absorption features that are manifested at 7 μm and longer wavelengths are described in the discussion of the thermal IR emissivity and micro-FTIR measurements below.

4.2. Thin section petrography and Micro-FTIR analysis

Plane polarized light photomicrographs of thin sections of the three types of tuffs reveal distinct differences between them as well as differences between the well-palagonitized hydro- and glaciovolcanic tuffs. The plane polarized light photomicrographs of sideromelane tuffs are dominated by sideromelane glass grains, some with dark coatings, and also host other minor (generally less than 5%) incidental phases- olivine, pyroxenes, plagioclase, and opaque phases. An example is the NMB12-14 sideromelane tuff in Fig. 6.

The brown/gray tuffs have sideromelane, more pervasive dark coatings and additional void-filling fine-grained smectites, and, in some instances, void-filling zeolites, again with minor incidental phases (Fig. 7). Some have minor palagonite rinds, but palagonite is generally not present.

The palagonite tuffs examined from the sampled tuff cones and the Split Butte tuff ring have extensive palagonite rinds and concomitant diminished amounts of sideromelane to virtually no sideromelane in some samples. These samples also have void-filling smectites and zeolites as well as minor (generally less than 5%) carbonate and incidental crystalline phases. The example of Pavant Butte sample PB13-013 in Fig. 8 displays just gel palagonites, but other samples show zoned rinds with inner lighter-toned gel palagonite and outer, darker-toned fibro-palagonites (essentially micro-crystalline smectite, e.g. Stroncik and Schmincke, 2002). The PB13-013 sample has relatively abundant void-filling smectite and

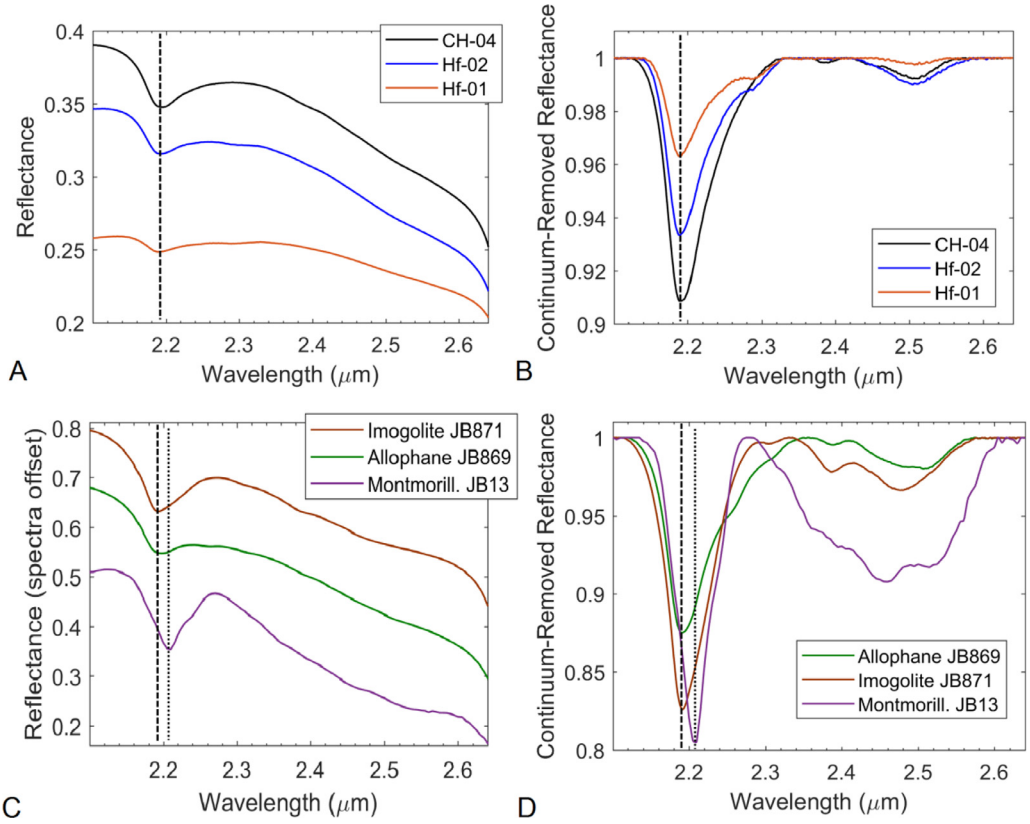

Fig. 4. (A) 2.1–2.64 μm region of glaciovolcanic palagonititized hyaloclastites from Helgafell (Hf) and Crazy Hills (CH). Dashed line indicates 2.2 μm absorption. (B) Continuum-removed versions of these spectra with dashed line indicating 2.2 μm absorption. (C) Laboratory spectra of poorly-ordered Al phyllosilicates, imogolite and allophane and well-ordered smectite montmorillonite. Dashed line indicates shorter band center of imogolite and allophane; dotted line indicates longer band center of montmorillonite. (D) Continuum-removed versions of.

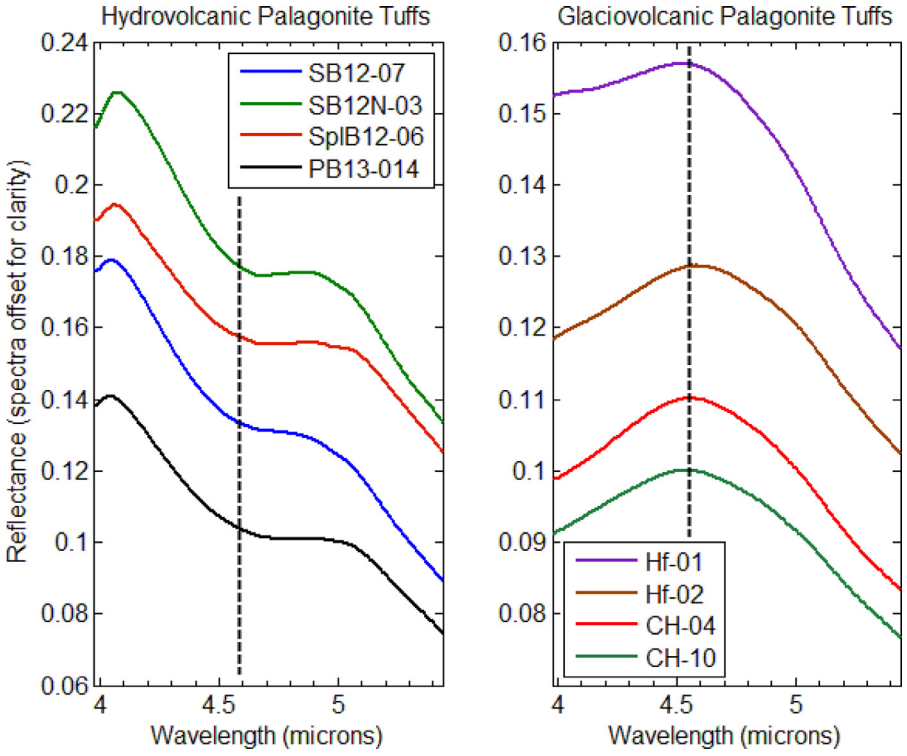

Fig. 5. (A) Hydrovolcanic palagonite tuffs over the 4.5 μm region showing 4.5 μm band indicated by the dashed line. (B) glaciovolcanic palagonitized hyaloclastites that display spectral convexity instead of an absorption in the 4.5 μm region.

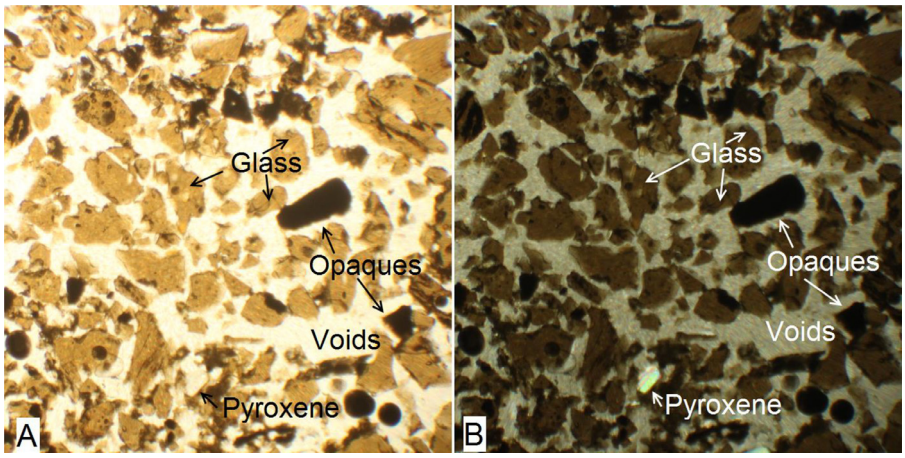

Fig. 6. (A) Plain-polarized light photomicrograph of NMB12-14 sideromelane tuff. (B) Cross-polarized light photomicrograph of NMB12-14 sideromelane tuff.

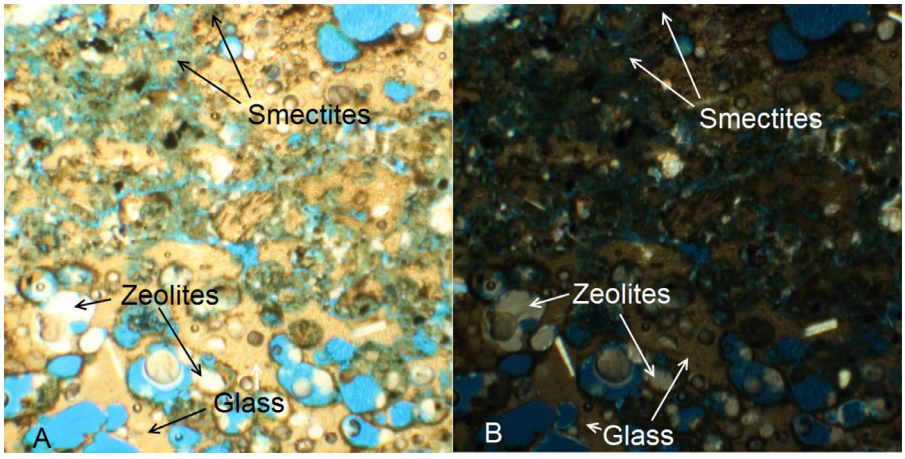

Fig. 7. (A) Pavant Butte gray tuff PB13-08 plain polarized light photomicrograph. Voids are blue. (B) PB13-08 cross polarized light photomicrograph. (For interpretation of the references to color in this figure legend, the reader is referred to the web version of this article.)

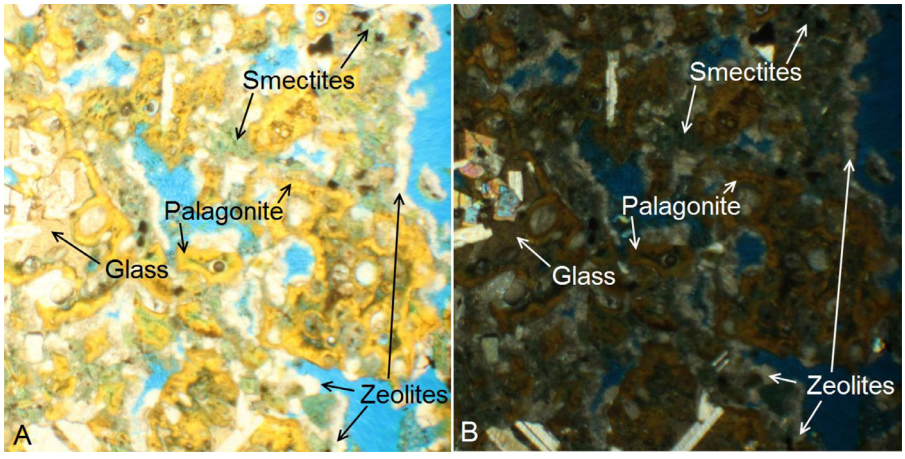

Fig. 8. (A) Plain polarized light photomicrograph of tuff cone palagonite tuff PB13-013. Voids are blue. (B) Cross-polarized light photomicrograph of PB13-013. Olivine, pyroxene, and plagioclase are brighter and colored. (For interpretation of the references to color in this figure legend, the reader is referred to the web version of this article.)

zeolite, but some of the sampled palagonite tuffs have diminished fractions of smectites (separate from those in the fibro-palagonite). Also, the smectites in plane polarized light in the Pavant Butte palagonite tuffs appear green but in other samples appear brown to red (e.g. the NMB12- 03 sample from N. Menan Butte shown in Fig. 9). The red smectites observed in thin section appear to be the equivalent of the "reddened smectite grain replacement (RSGR)" described by Walton and Schiffman (2003), although in the samples examined here the smectites appear to be void-filling rather than grain-replacing phases.

The glaciovolcanic sites examined do not have brown/gray tuffs, as defined above as consisting principally of glass and smec-

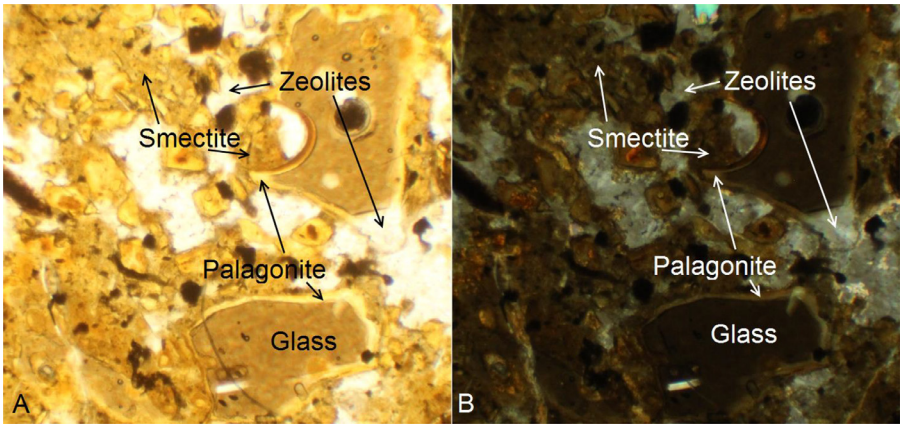

Fig. 9. (A) Plain-polarized light photomicrograph of tuff cone palagonite tuff NMB12-03 with red void filling smectites. (B) Cross-polarized light photomicrograph of NMB12-03. (For interpretation of the references to color in this figure legend, the reader is referred to the web version of this article.)

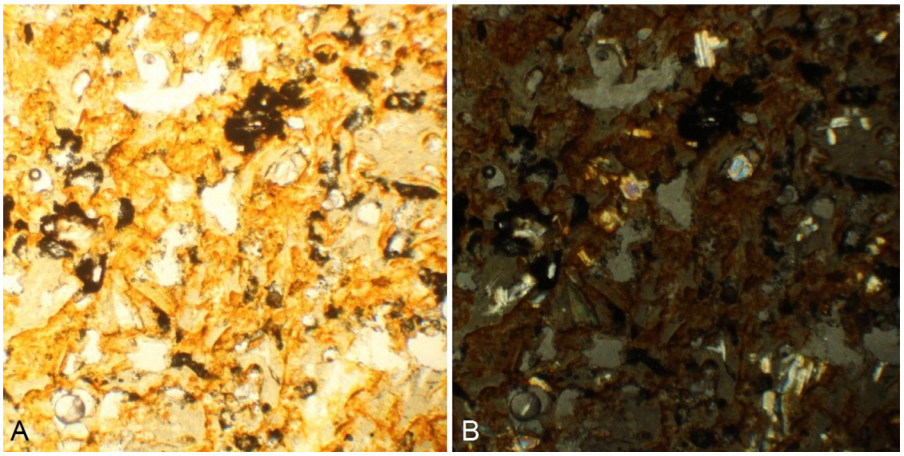

Fig. 10. (A) Plain-polarized light photomicrograph of glaciovolcanic palagonite tuff CH-04 consisting principally of sideromelane palagonite, voids, and minor olivine, pyroxene, and plagioclase (brighter colored grains in the cross-polarized light view in (B)).

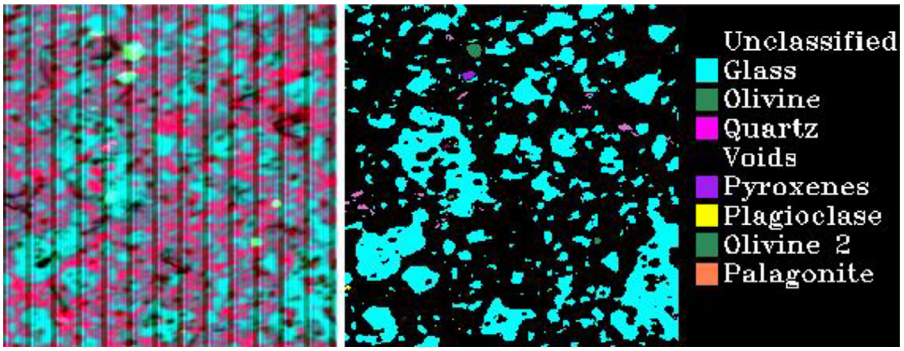

Fig. 11. (A) Micro-FTIR composite (bands centered at 1250, 950 and 450 cm^{-1}) of NMB12-01. (B) SAM class map of that same view.

tites. Instead they consist of sideromelane with increasing amounts of palagonite without signs of void-filling smectites or zeolites (Fig. 10).

Comparing the optical plane polarized light photomicrographs of thin sections to the hyperspectral images from the micro-FTIR of portions of those same thin sections allows for the extraction of reflectance spectra (in the 2.5–14.5 μm range) of individual grains, and grain components. It also allows for the mapping of tuff components at the microscopic level. Fig. 11A shows a composite of a micro-FTIR view of the NMB12-01 sideromelane tuff, along with a SAM class map of that view (Fig. 11B). Sideromelane tuff samples are dominated by voids and unclassified groundmass, but otherwise consist mainly of unaltered glass grains with minor occurrences of opaque minerals, olivine, and pyroxene.

In Fig. 12, the micro-FTIR composite and SAM class map of brown tuff PB13-08 are shown. Smectites are absent from the sideromelane tuffs but constitute from 9 to 26% of gray tuffs based on thin section point counts and from the micro-FTIR classifications. In Fig. 13, the micro-FTIR composite and SAM class map of palagonite tuff SB12N-03 are shown. Smectites are still present in the hydrovolcanic palagonite tuffs (note discussion of differences in palagonitized glaciovolcanic hyaloclastites below), but are in lower abundance than palagonite and zeolites. Depending on the level of

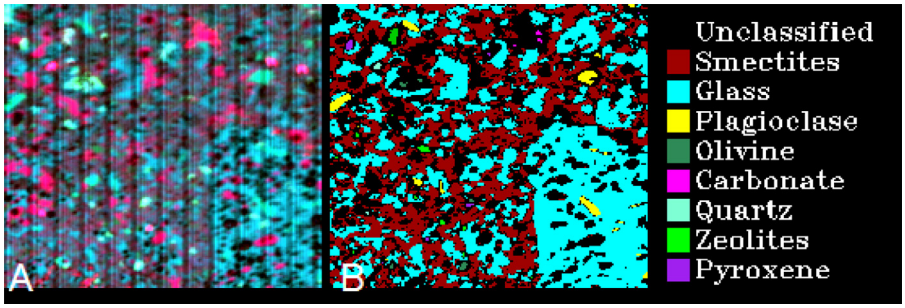

Fig. 12. (A) Micro-FTIR composite (bands centered at 1250, 950 and 725 cm^{-1}) of PB13-08. (B) SAM class map of the same view. Note abundance of smectites vis-à-vis what is in the sideromelane tuff.

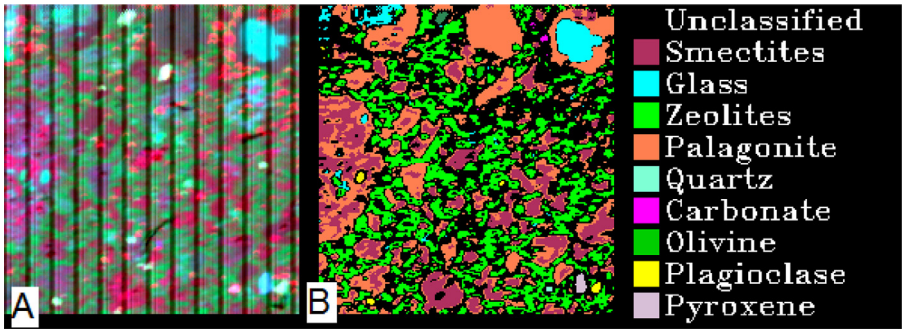

Fig. 13. (A) Micro-FTIR composite (bands centered at 1250, 950 and 450 cm^{-1}) of SB12N-03. (B) SAM class map of the same view. Note presence of abundant palagonite and zeolites and reduced fraction of glass and smectites vis-à-vis what the sideromelane and gray tuffs.

palagonitization, glass might be present only as a minor phase, if present at all.

Spectra extracted from the micro-FTIR data provide information on the reflectance of pure phases. Glass grains (blue spectrum in Fig. 14) have a symmetrical reflectance peak with a reflectance maximum (emissivity minimum) centered from 1010 to 980 cm^{-1} (9.9–10.2 μm) that has minor variations from sample to sample. In the palagonitized samples, palagonite rinds form around the glass grains (very apparent in Figs. 8 and 9) and in the SAM class map of Fig. 13B, notably the grain in the upper right of that figure. The palagonite rinds (red spectrum in Fig. 14) have a 1002.85 cm^{-1} (9.97 μm) reflectance peak (emissivity minimum), narrower width than the glass grains, have a 3602.5 cm^{-1} (2.78 μm) reflectance minimum attributable to the water in the palagonite, and a weaker band at 1681.69 cm^{-1} (5.95 μm) also attributable to palagonite hydration. The palagonite spectra are very similar to smectite spectra (purple spectrum in Fig. 14). The micro-FTIR composites of palagonite tuffs such as that of SB12N-03 shown in Fig. 13A have a substantial green component (in the 1250, 950, 750 cm^{-1} band combination), which has a spectrum (black spectrum in Fig. 14) (with a 1025.99 cm^{-1} reflectance maximum and reflectance minima at 3625.67 and 1673.98 cm^{-1} (the latter two being water absorption features)) consistent with a zeolite phase.

4.3. MWIR emission spectroscopy

Our companion paper (Farrand et al., 2016), notes that MWIR emissivity spectra of glass-rich, minimally altered sideromelane tuffs do not display the "U" shaped SiO_4 stretching band of the glass grains seen in the Micro-FTIR reflectance spectra (Fig. 14, blue spectrum). Instead, the tuff hand samples display a double absorption that was previously described for glass rinds of basalt flows by Crisp et al. (1990). Crisp et al. (1990) attributed the development of bands centered initially from 9.2 to 9.25 μm and from 10.5 to 10.8 μm (and with age shifting to, respectively, 9.1–9.15 μm and 10.7–10.9 μm) to the incipient development of SiO_4 sheet and chain structures, respectively. Among the samples we have examined, the SiO_4 sheet feature has emissivity minima from 1047 to 1037 cm^{-1} (9.5–9.6 μm) and the SiO_4 chain feature from 912 to 904 cm^{-1} (10.96–11.1 μm).

The SiO_4 stretching feature of the brown/gray tuffs (Fig. 15A) and the palagonite tuffs (Fig. 15B) are similar in that they are more "V" shaped than those of the sideromelane tuffs. For both sets of tuffs, the emissivity minimum of this feature is centered near 1035 cm^{-1} (9.7 μm). Both sets of tuffs also generally have a SiO_4 bending feature at approximately 452 cm^{-1} (22 μm). It is noteworthy that, to visual inspection, this is a single feature and not a double feature. Dioctahedral clays, such as nontronite, have a double feature in the 380–570 cm^{-1} (26.3–17.5 μm) region, while trioctahedral clays, such as saponite, have a single SiO_4 bending feature in this region (Michalski et al., 2006).

The more highly altered palagonite tuffs are also more likely to have a sharp feature near 880 cm^{-1} (11.3 μm) and a stronger, broader band with an emissivity minimum near 1540 cm^{-1}; both features are attributed to the presence of carbonate minerals (some of the brown/gray tuff samples also have these carbonate features).

Approximate mineral abundances of altered glass samples are derivable from the thermal emissivity spectra of the bulk samples by using the linear deconvolution methodology of Ramsey and Christensen (1998). We used the amended procedure developed by Rogers and Aahronson (2008) that utilizes a non-negative least squares approach. The deconvolution was performed over the 1400–410 cm^{-1} (7.1–24 μm) range (higher wavenumbers were not used in order to mitigate grain size effects that become stronger at higher wavenumbers). As noted in the references cited above, the ability to assess the amount of any given phase using linear deconvolution should only be trusted to within approximately the 5% level; thus, phases detected at less than 5% abundance may or may not be present. Average point count and deconvolution results

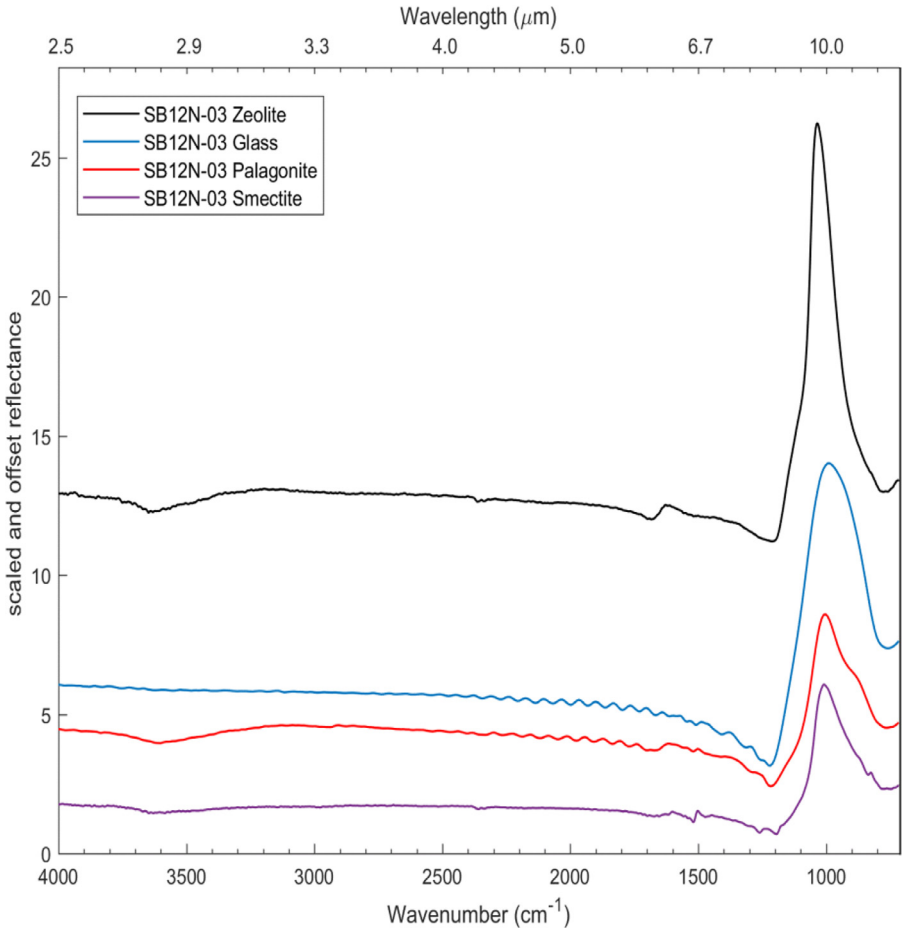

Fig. 14. Reflectance spectra of main components identified in Micro-FTIR image cubes. (For interpretation of the references to color in this figure, the reader is referred to the web version of this article.)

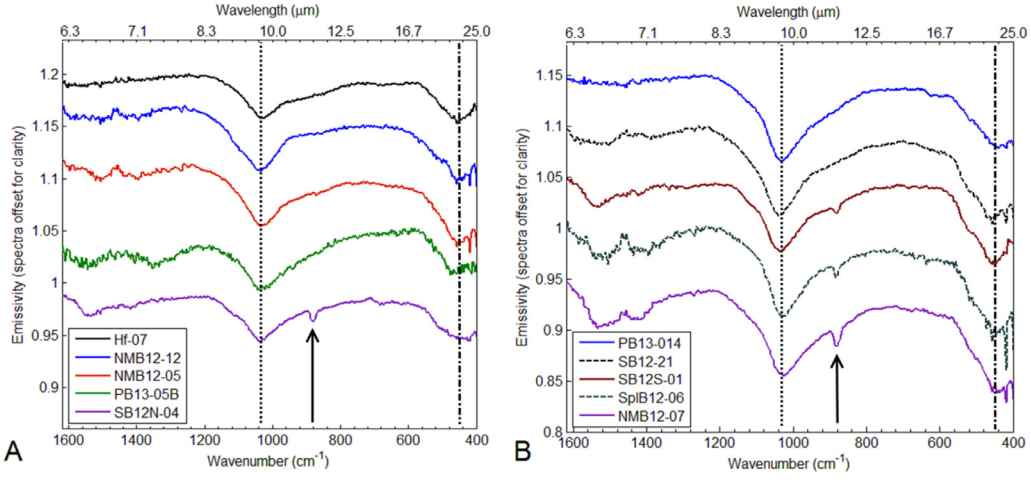

Fig. 15. (A) Representative brown/gray tuff emissivity spectra. Dotted line indicates SiO_4 stretching feature. Dash-dot line indicates SiO_4 bending feature. Arrow points out carbonate absorption. (B) Representative emissivity spectra of palagonite tuff samples. Spectra of emissivity spectra are included in table form in supplementary Table 3. (For interpretation of the references to color in this figure legend, the reader is referred to the web version of this article.)

for representative palagonite tuffs are shown in Fig. 16 in pie chart form. The MWIR palagonite spectra, derived from the micro-FTIR, and those of the library smectite spectra, are very similar (e.g., Fig. 14); thus, palagonite and smectites are grouped together in Fig. 16 in a single color for more ready comparison of the combined palagonite + smectite group in the point count and deconvolution results.

4.3.1. Comparison of petrography and MWIR linear deconvolution

Above we alluded to differences between the palagonitized hydrovolcanic and glaciovolcanic tuffs. This difference is evident in comparing the relative abundances of component phases in the two hydrovolcanic palagonite tuffs in Fig. 16A/D and B/E against that of the Helgafell Hf-01 partially palagonitized hyaloclastite in Fig. 16C/F. It is apparent from results of both the petrographic and

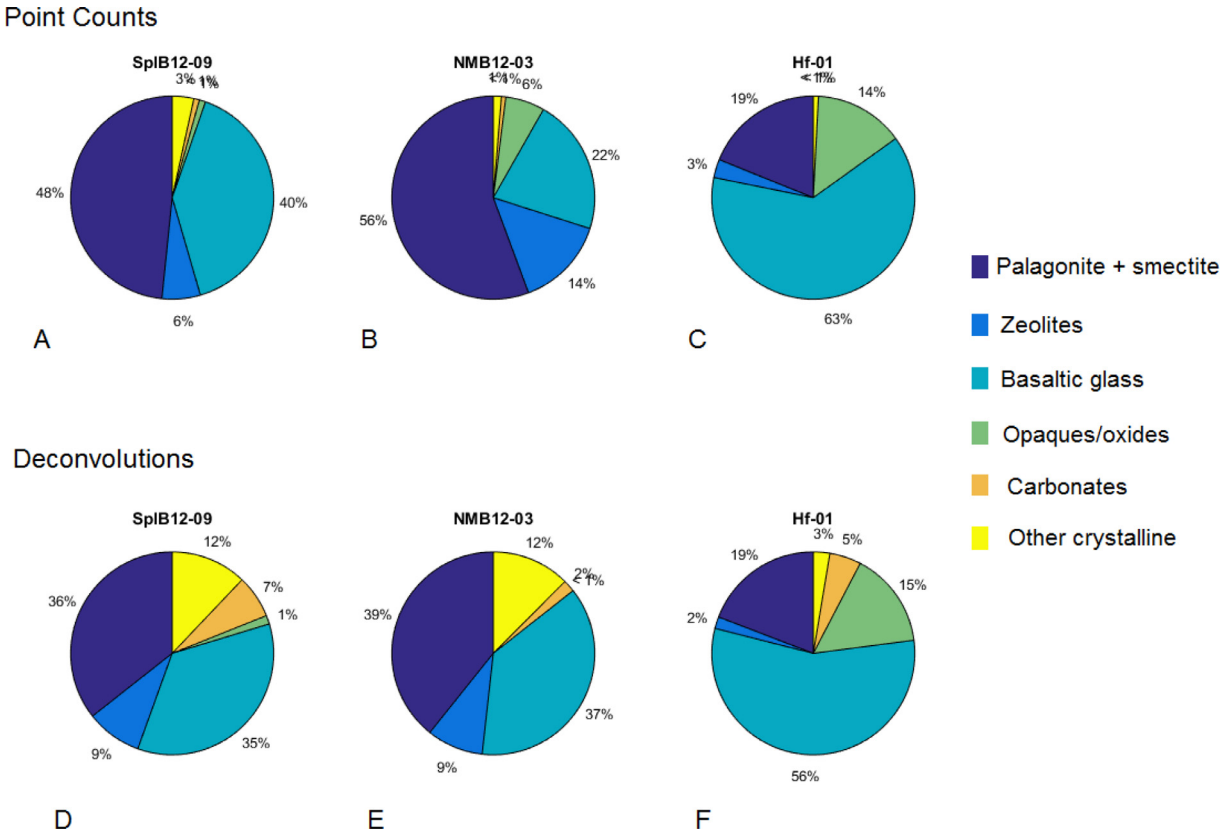

Fig. 16. Pie charts of representative palagonite tuffs. (A)–(C) are point count results and (D)–(F) are results of linear deconvolution of MWIR emissivity spectra of bulk samples.

the linear deconvolution analyses that there are notable differences between the relative amounts of the alteration products formed in the hydrovolcanic palagonite tuffs vs. those from the glaciovolcanic Helgafell hyaloclastite ridge. These notable differences include:

- More zeolites in the hydrovolcanic palagonite tuffs relative to the palagonitized glaciovolcanic hyaloclastites;
- Greater fractions of glass in the palagonitized Helgafell tuffs relative to the hydrovolcanic hyaloclastites;
- Greater fractions of opaque minerals (as derived from point counting)/oxides (as derived from the linear deconvolution) in the glaciovolcanic hyaloclastites.

4.4. X-Ray diffraction

XRD analysis was performed on a number of samples with the objective of confirmatory identification of alteration phases. Given the poorly crystalline nature of most of the samples, alteration phases were confidently identified in only a subset of the samples. Samples with positive identifications of smectites or zeolites are listed in Table 2. Representative XRD traces are shown in Fig. 17.

4.5. Mössbauer spectroscopy results

Mössbauer spectroscopic analysis was performed on the hydrovolcanic gray and palagonite tuffs and Helgafell hyaloclastites noted in Table 1. As with the previously discussed analysis methods, there are clear differences between the palagonite and the brown/gray tuffs. Fig. 18 shows representative Mössbauer spectra of two palagonite tuff samples and two brown/gray tuff samples along with the curve fitting results assigning the relative distribution of Fe between the component Fe-bearing phases. The palagonite tuff samples are dominated by octahedrally coordinated Fe^{3+} that is likely either in superparamagnetic nanophase Fe, nominally in the palagonite, or split between palagonite and smectite. Brown/gray tuffs have a stronger contribution from Fe^{2+} in the low isomer shift (IS) distribution, which has parameters often seen in glasses. However, generally speaking, there is a much greater proportion of this low IS component in minimally altered, gray, and gray/brown tuffs.

The Fe^{2+} in all of the samples displays a range of IS and quadrupole splitting (QS) values (see supplementary Table 1). Basaltic glass in palagonitic tephra from Mauna Kea, Hawaii, have been investigated with Mössbauer spectroscopy (Bell et al., 1993; Morris et al., 1993, 2000, 2001). Morris et al. (2008) summarize the results from these studies and from investigations of synthetic basaltic glass. They report average parameters of IS = 0.30 ± 0.02 mm/s and QS = 1.14 ± 0.08 mm/s for Fe^{3+} in basaltic glass. Only the minimally altered hyaloclastite Hf-06 has parameters close to that range (Supplementary Table 1a). However, many of the tuffs and hyaloclastites contain significant amounts of Fe^{2+}in a phase (Supplementary Table 1b) that has Mössbauer parameters similar to those reported for Fe^{2+} in basaltic glass, IS = 1.04 ± 0.03 mm/s and QS = 1.98 ± 0.04 mm/s (Morris et al., 2008). However, we note that the Mössbauer parameters reported for basaltic glass overlap with the parameter space for clay minerals and pyroxenes. Some contribution to the Fe^{2+} signal could potentially come from minor constituents such as olivine and pyroxene although thin section point counts indicate that these phases are only present in minor quantities (generally on the order of 1–2%). This may not be a contradiction when one takes into account that the Mössbauer signal only accounts for Fe-bearing phases and these phases may therefore find larger representation in the Mössbauer signal than the overall bulk signal.

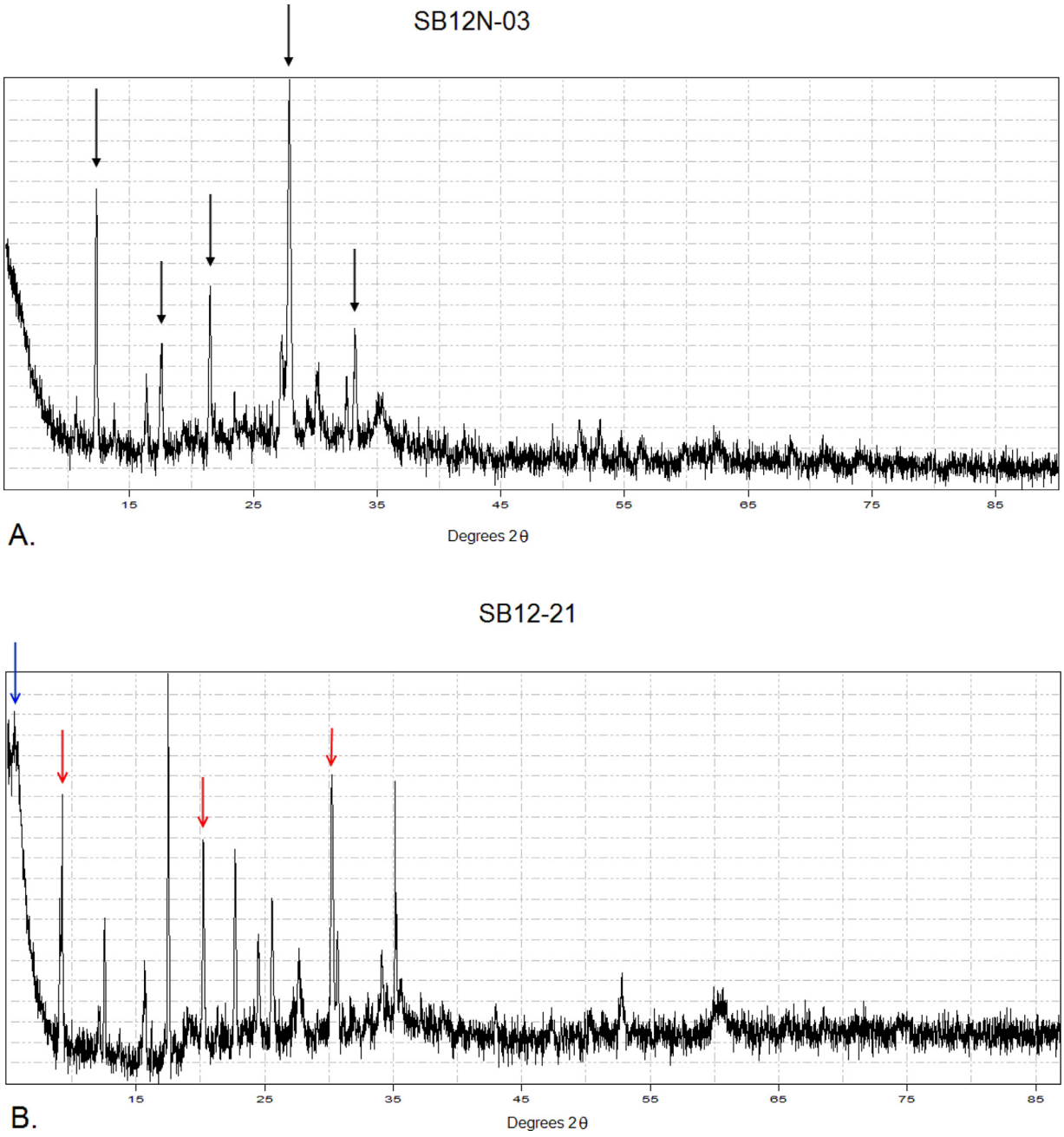

Fig. 17. (A) XRD trace of Sinker Butte palagonite tuff SB12N-03. Black arrows indicate XRD peaks of phillipsite. (B) XRD trace of Sinker Butte palagonite tuff SB12-21. Blue arrow indicates nontronite peak. Red arrows indicate chabazite peaks. Additional peaks are from incidental crystalline phases. (For interpretation of the references to color in this figure legend, the reader is referred to the web version of this article.)

With regards to the glaciovolcanic hyaloclastite samples, even the most highly oxidized of these, such as the palagonitized Helgafell sample Hf-02, still only has an Fe^{3+} contribution that is on a par with that of the hydrovolcanic brown/gray tuffs (Supplementary Table 1a). However, this accords well with the observation above in Section 4.3.1 that the palagonitized glaciovolcanic hyaloclastites have higher fractions of glass than the examined hydrovolcanic palagonite tuffs.

4.6. XRF/wet chemistry results

There have been numerous studies examining chemical changes in glassy basaltic tephras as they alter to palagonite (recent syntheses include Stroncik and Schmincke, 2001, 2002 and Pauly et al., 2011). Our results are in accordance with these past studies with regards to increases in hydration (as measured through loss-on-ignition, LOI) and oxidation (as determined through iron titration and indicated most prominently in the increase in the $Fe_2O_3/(FeO + Fe_2O_3)$ ratio). These results are discussed below in the Discussion section in conjunction with ways that the chemistry correlates with reflectance spectroscopy. Major element and LOI and iron titration results for samples noted in Table 2 are provided in a supplementary table (supplementary Table 4).

5. Synthesis of results/discussion

To understand the nature of materials from a rover-perspective generally requires the integration of results from more than one analysis technique. This is true also with the analysis of the al-

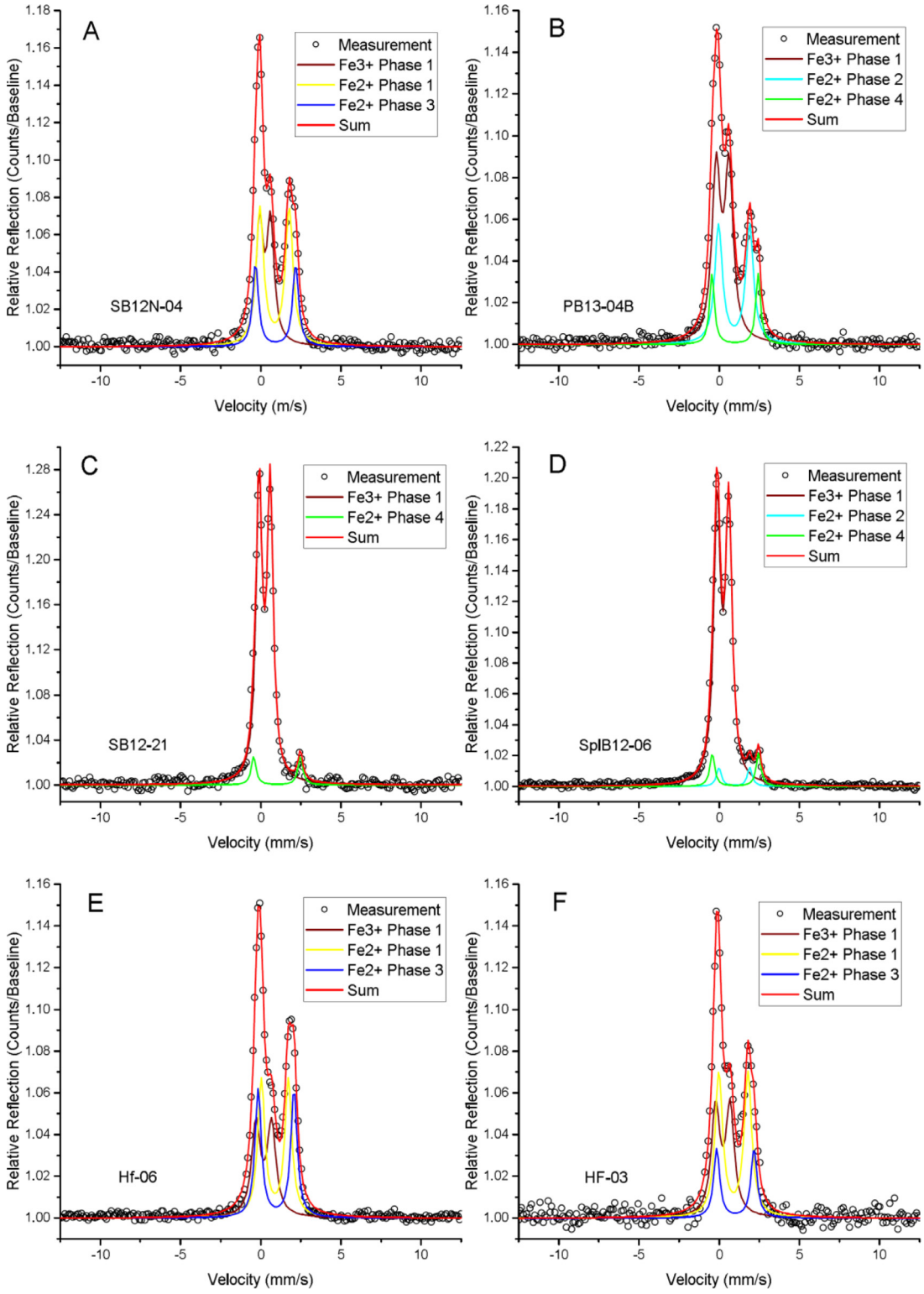

Fig. 18. Mössbauer spectra of hydrovolcanic brown/gray tuffs (A) SB12N-04, (B) PB13-04B; palagonite tuffs (C) SB12-21, and (D) SplB12-06; and glaciovolcanic hyaloclastites (E) minimally altered Hf-06, (F) partially palagonitized Hf-06. Curve fit Fe-bearing phases are shown with their relative percentages noted in the legends. All samples shown were measured on a MIMOS-2.

tered basaltic tuffs examined in this study. From an initial visual inspection of outcrops containing altered basaltic tuffs (e.g., Fig. 1), preliminary assessments can be made of whether the outcrop is light- or dark-toned and of its color. With darker ash beds or tuffs being darker-toned and lighter toned tuffs having undergone more alteration. However, more detailed understanding of the nature of alteration products requires the use of more sophisticated analysis techniques.

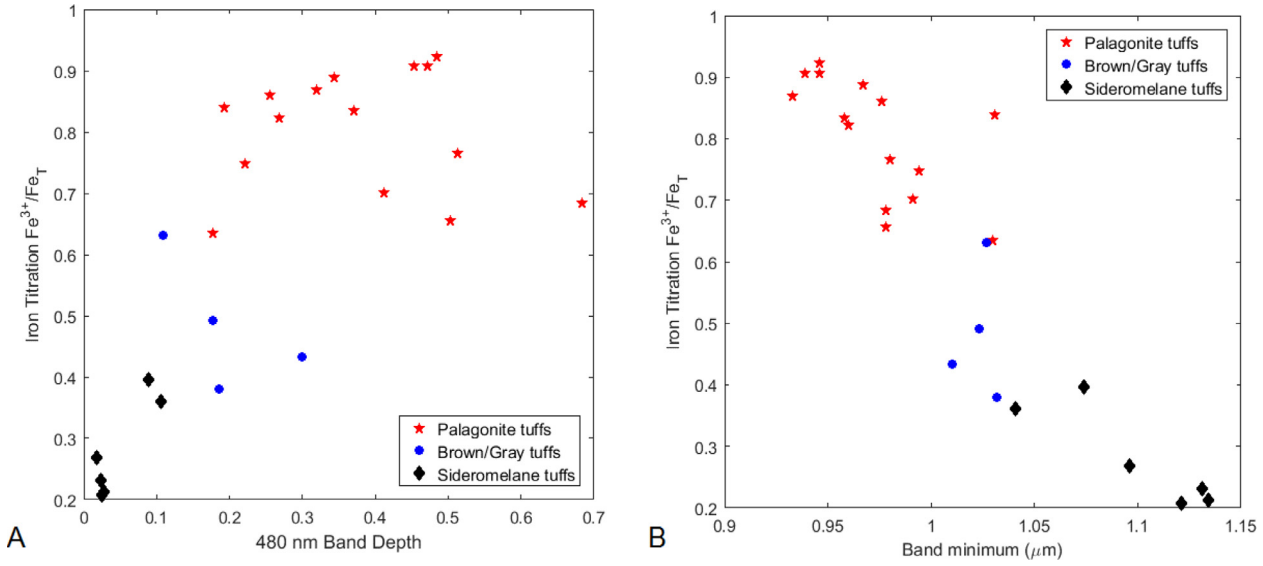

Fig. 19. (A) Iron titration derived Fe^{3+}/Fe_{Total} vs. 480 nm band depth with samples grouped according to tuff type. (B) Iron titration derived Fe^{3+}/Fe_{Total} vs. 1 μm band minimum position with samples grouped according to tuff type.

5.1. Iron-bearing minerals

Applying VNIR-SWIR reflectance spectroscopy provides more information on the types of iron bearing phases present in the form of the shape, position, and strength of iron charge transfer and crystal field absorption bands in the reflectance spectra. Unaltered to minimally altered tuffs have broad iron crystal field absorption bands centered from 1.05 to 1.15 μm and near 2 μm (Fig. 2A). The more highly oxidized palagonite tuffs have narrower iron crystal field bands with the "1 μm" band center shifted to shorter wavelengths as a result of the development of ferric oxide or oxyhydroxide minerals (Farrand and Singer, 1992). However, the Mössbauer spectroscopy results indicate that these ferric oxide or oxyhydroxide minerals are still nanocrystalline based on the strength of the nanophase iron doublet in the Mössbauer spectra of the highly palagonitized tuffs (e.g., Fig. 18C and D). TIR emission (or reflectance in the same MWIR spectral region) spectroscopy is more sensitive to the silicate bonds that are present, and clearly distinguishes between the more glass-rich spectra (e.g., Fig. 14, blue spectrum) with the more "U" shaped SiO_4 stretching feature centered near 10.1 μm (990 cm^{-1}) for fresh glass surfaces and with a doublet as discussed by Crisp et al. (1990) and Farrand et al. (2016) and spectra of samples with more highly polymerized minerals (with a more "V" shaped SiO_4 stretching feature.

The oxidation of the samples with increasing alteration is also apparent in the iron titration determined Fe^{3+}/Fe_{Total} ratios and as is illustrated in Fig. 19A, with increasing iron oxidation, the 480 nm band depth increases. In Fig. 19B, an even more linear relationship is observed in the plot of Fe^{3+}/Fe_{Total} vs. "1 μm" crystal field band position. The plots in Fig. 19 also illustrate separation between the sideromelane, gray–brown, and palagonite tuffs discussed previously. The trends in Fig. 19, of increasing 480 nm band depth with iron oxidation (Fig. 19A) and the shift to shorter band centers of the iron crystal field band with increasing iron oxidation, illustrates the formation of (nanophase, based on Mössbauer results) ferric oxides or oxyhydroxides in the tuffs with oxidation. As noted above in Section 4.1.1, Fe-bearing glasses have this iron crystal field band centered from 1.05 to 1.15 μm. The shorter iron crystal field band centers in palagonite tuffs (around 0.95 μm) are more consistent with oxyhydroxides such as goethite or ferrihydrite or some mixture of these minerals and glass, or even shorter band center minerals such as hematite, albeit in a nanocrystalline form.

5.2. Hydration of samples

The increasing hydration of the samples with increasing alteration is indicated both by the development and growth of H_2O and OH overtone features centered near 1.4 and 1.9 μm in the VNIR-SWIR reflectance spectra (Fig. 2B and C), by the growth of the 6 μm H–O–H bending fundamental absorption band, and by the laboratory determined loss-on-ignition (LOI) measurements. Comparing these two sets of measurements in Fig. 20, reveals differences between the three sets of tuffs and between the hydrovolcanic tuffs and the smaller set of glaciovolcanic hyaloclastites that were examined from Crazy Hills and Helgafell. Fig. 20A plots 1.9 μm band depth vs. loss on ignition for the hydrovolcanic geochemically analyzed samples. Only the hydrovolcanic samples are plotted in Fig. 20A because of notable differences in the level of hydration between the altered hydro- and glaciovolcanic tephras. Fig. 20B plots 1.9 μm band depth vs. 6 μm band depth of palagonite tuffs formed by hydrovolcanism and those formed at Crazy Hills and Helgafell by glaciovolcanism. The lower hydration feature band depths of the palagonitized glaciovolcanic hyaloclastites relative to the hydrovolcanic palagonite tuffs is attributed primarily to the presence of zeolites in the latter, but not in the former. Pauly et al. (2011) also reported on subglacially-formed, palagonitized samples from the Mosfell and Ingólfsfjall tuyas in Iceland and found abundant zeolites in the former, but not the latter; thus, the relation between hydrovolcanic and glaciovolcanic palagonites and the extent to which zeolites are formed in them appears to be more complicated than the simple case examined here with the Crazy Hills and Helgafell samples. Further work on this topic, such as that in a recent study by Ackiss et al. (2017), is required to provide additional information a palagonitized subglacial tuffs and hyaloclastites produced in a variety of glaciovolcanic settings.

5.3. Smectites

The analysis methods that were best suited for determining the identity of smectites formed in the studied samples were VNIR-SWIR reflectance spectroscopy and XRD. However, clear nontronite diffraction peaks were definitively observed in only a relatively

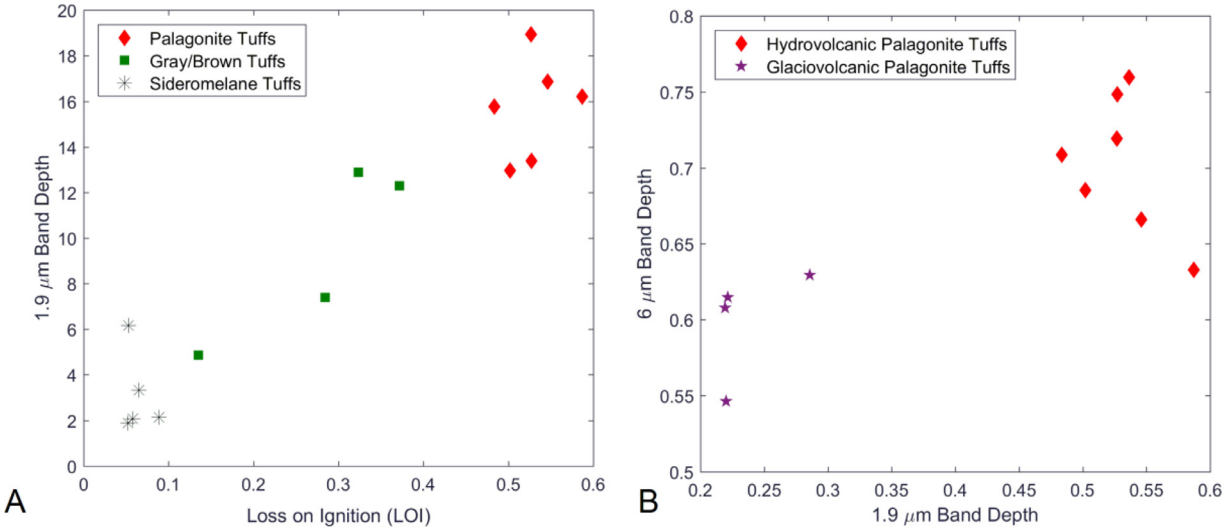

Fig. 20. 1.9 μm band depth vs. LOI for chemically analyzed tuff samples, separated by symbol into distinct groups. (B) 1.9 μm band depth vs. 6 μm band depth for representative hydrovolcanic and glaciovolcanic palagonite tuffs.

small number of samples while a distinct 2.29 μm absorption was observed in many of the gray–brown and palagonite tuff samples. An aluminous smectite phase was not detected in any of the XRD patterns; however, again, in the reflectance spectra a weak 2.2 μm absorption, associated with an Al–OH overtone feature, was observed in a number of sample spectra.

The 2.29 μm band, which we associate with nontronite or a related Fe-bearing smectite, was not observed in the Crazy Hills or Helgafell glaciovolcanic palagonitized hyaloclastites. However, in their study of a palagonitized hyaloclastite from the Thórólfsfell hyaloclastite ridge in Iceland Bishop et al. (2002) found evidence for the presence of both Al and Fe-bearing smectites. However, they did not report on evidence of zeolites in the Thórólfsfell samples. As with the non-detection of zeolites in the Crazy Hills and Helgafell samples, we are hesitant to assign any universal lack of association of nontronite with glaciovolcanic palagonitized hyaloclastites; however, for the samples examined, zeolites and nontronite (or an associated phase or poorly crystalline version thereof) were not observed.

5.4. Summary

While relatively unaltered tephra, and tephra altered to well-indurated palagonite tuff, from hydro- and glaciovolcanic eruptions are well-documented, less well-documented are smectite-bearing, but largely palagonite-free, tuffs. We find that these tuffs are distinct from minimally altered sideromelane tuffs and hydrothermally altered palagonite tuffs. They are distinct in terms of color, petrographic character, VNIR – SWIR reflectance, and Mössbauer spectroscopy from sideromelane and palagonite tuffs.

The smectite-bearing tuffs, with little to no palagonite, are gray to brown in color compared to the black or gray of sideromelane tuffs or the light-toned buff to light brown of palagonite tuffs. Petrographic differences between the three types of tuff are evident both in thin section and in the micro-FTIR hyperspectral data cubes. The brown/gray tuffs do not display palagonite rinds on the border of sideromelane (glass) grains, but do have void-filling smectites, and zeolites are present in some samples as well.

The brown/gray tuffs are less oxidized and less hydrated than the palagonite tuffs as evidenced both by laboratory measurements such as, respectively, iron titration derived Fe^{3+}/Fe_{Total}, and loss-on-ignition, by spectral reflectance characteristics including the VNIR 480 nm band depth or iron crystal-field band minimum position. The brown/gray tuffs are also distinct from palagonite tuffs in terms of their Mössbauer spectra and band fitted phase abundances with the former having higher fractions of low IS glass-like distributions.

The brown/gray and palagonite tuffs have very similar-appearing MWIR emissivity spectra due in large part to the spectral similarity of zeolites, smectites, and palagonite in the 8–13 μm SiO_4 stretching region.

There are also spectral, mineralogic, and petrographic differences between the hydrovolcanically formed palagonite tuffs and palagonitized hyaloclastites from the two subglacially formed hyaloclastite ridges that were sampled. The samples from the two hyaloclastite ridges display a continuum from minimally altered, sideromelane dominated to more palagonitized samples. Petrography indicates little or no void-filling smectites or zeolites. The reflectance spectra of the samples confirm these differences. Hydrovolcanic palagonite tuffs have 2.5 and 4.5 μm bands that we attribute primarily to the presence of zeolites. These bands are weak to absent in the reflectance spectra of the palagonitized glaciovolcanic hyaloclastites. The palagonitized glaciovolcanic hyaloclastites are also less hydrated than the hydrovolcanic palagonite tuffs- illustrated in Fig. 20 by the lower loss-on-ignition values and lower 1.9 μm band depths.

The “outer slope hyaloclastites” described by Jakobsson and Gudmundsson (2008) are one example of the brown/gray tuffs described here. Jakobsson and Gudmundsson (2008) cited the recent Gjalp hyaloclastite mound formation and its development of palagonite in the first 1–2 years as an example of the hydrothermal, and relatively rapid, development of palagonite compared to the “outer slope hyaloclastites”, which they described as altering through low temperature diagenesis over thousands of years. This description matches the gray mantling tuffs as in Fig. 1A for which the PB13-4B sample is an example. However, in our field work we also found brown tuffs in the middle of tuff ring and tuff cone sequences as in Fig. 1C and D. A possible explanation for how these tuffs can have smectites without extensive palagonitization is that they occur adjacent to palagonitized layers. The palagonitized layers would have been deposited with steam, buried by additional tephra layers, kept warm and palagonitized relatively rapidly. Adjacent layers above or below them could have been deposited without steam but could still have been heated and received diffused

water from the layers below or above. The alteration temperatures would have been below that seen for palagonitized deposits, but sufficient over time to produce some smectite development.

The differences between the hydrovolcanic tuffs and the altered hyaloclastites from the two hyaloclastite ridges that were examined might also be attributable to time of alteration. Subaerially deposited ash beds, as at the hydrovolcanic edifices examined in this study, have time to alter without aggressive cooling (as for subaqueously deposited ash beds). Tindar deposits are formed within ice sheets and are ultimately subject to cooling from the surrounding ice. Zeolite bearing hyaloclastites have been described in association with tuya deposits (e.g., Pauly et al., 2011). However, tuyas, by definition, breach the top of the ice sheet. We were not able to examine these deposits as part of this work, but we posit that the zeolite-bearing palagonitized hyaloclastites described by Pauly et al. (2011) were part of subaerially deposited beds.

The tephras, tuffs, and alteration products discussed here likely also exist on Mars. Brož and Hauber (2013) have identified a number of candidate tuff rings and tuff cones. Farrand et al. (2008) and Ackiss et al. (2016) have suggested some of the hills in the southern Sisyphi Montes as possible tuyas and hyaloclastite mounds. There have also been suggestions of larger scale water-magma interactions in a number of studies cited by Head and Wilson (2007). Given presumed cold surface temperatures on even early Mars, hydrovolcanic materials erupted onto the surface and rapidly buried by other ashes might have been subjected to a shorter time for hydrothermal alteration and produced in an intermediate alteration product resulting from water-magma interactions, such as the brown/gray tuffs described here, might be more common on Mars than fully palagonitized tuffs.

6. Conclusions

This study has provided information on the types of analysis techniques that might prove most useful in distinguishing between different types of tuff produced by hydro- or glaciovolcanic activity. As noted above, in the MWIR emissivity measurements, the palagonite and brown/gray tuffs had similar spectra in the 8–14 μm region, but were distinct in terms of VNIR-SWIR reflectance and Mössbauer spectra. They were also distinct in terms of petrographic characteristics; however, thin section analysis of martian samples is currently restricted to analysis of SNC meteorites and to potential future Mars sample return samples. Measures of chemistry, especially with regards to iron oxidation and water content were also useful discriminating factors between the different tuff types.

The types of materials associated with hydro- and glaciovolcanic features, as characterized in this study, likely exist on the martian surface and in future exploration of the surface of Mars might be recognized by rover-hosted instrumentation using analysis approaches used in this study. The recognition of materials produced by water-magma interactions would then provide important details on the hydrologic and volcanic history of the region(s) being studied.

Acknowledgments

Funding for initial work on this study was provided through the NASA Mars Fundamental Research Program grant number NNX12AH92G. We thank Dr. V. Hamilton of SWRI and M. Osterloo of LASP for collecting emissivity measurements on a number of samples. We also thank Dr. Stan Mertzman of Franklin & Marshall College for carrying out XRF analyses and providing information on measurement procedures. Thanks also to Dr. Deanne Rogers of Stony Brook University for providing linear deconvolution software. Finally thanks ot Dr. Takahiro Hiroi of Brown University for carrying out reflectance measurements at RELAB and providing information on measurement procedures. C. Schröder acknowledges funding from the UK Space Agency through grant ST/R001278/1 administered by the Science and Technology Facilities Council.

Supplementary materials

Supplementary material associated with this article can be found, in the online version, at doi:10.1016/j.icarus.2018.03.005.

References

Ackiss, S.E., Campbell, A., Horgan, B., Seelos, F.B., Wray, J.J., Michalski, J.R., 2016. Mineralogical evidence for subglacial volcanoes in the sisyphi montes region of Mars. In: Proceedings of the 47th Lunar and Planetary Science Conference abstract #1305.

Ackiss, S.E., Horgan, B., Gudnason, J., Haberle, C., Thorsteinsson, T., Thordarson, T., 2017. The mineralogic variability of Icelandic palagonites: An analog study for Mars. In: Proceedings of the Lunar and Planetary Science XLVIII abstract # 2500.

Adams, J.B., 1975. Interpretation of visible and near-infrared diffuse reflectance spectra of pyroxenes and other rock-forming minerals. Infrared and Raman spectroscopy of lunar and terrestrial minerals, pp. 91–116.

Adams, J.B., Smith, M.O., Gillespie, A.R., 1993. Imaging spectroscopy: Interpretation based on spectral mixture analysis. In: Pieters, C.M., Englert, P.A.J. (Eds.), Remote Geochemical Analysis: Elemental and Mineralogical Composition. Cambridge University Press, New York, pp. 145–166.

Allen, C.C., Gooding, J.L., Jercinovic, M., Keil, K., 1981. Altered basaltic glass: a terrestrial analog to the soil of Mars. Icarus 45, 347–369.

Bandfield, J.L., Hamilton, V.E., Christensen, P.R., 2000. A global view of Martian surface compositions from MGS-TES. Science 287, 1626–1630.

Bell III, J.F., Morris, R.V., Adams, J.B., 1993. Thermally altered palagonitic tephra: a spectral and process analog to the soil and dust of Mars. J. Geophys. Res. 98, 3373–3385.

Bish, D.L., Blake, D.F., Vaniman, D.T., Chipera, S.J., Morris, R.V., Ming, D.W., Treiman, A.H., Sarrazin, P., Morrison, S.M., Downs, R.T., Achilles, C.N., Yen, A.S., Bristow, T.F., Crisp, J.A., Morookian, J.M., Farmer, J.D., Rampe, E.B., Stolper, E.M., Spanovich, N., MSL Science Team, 2013. X-ray diffraction results from mars science laboratory: mineralogy of rocknest at gale crater. Science 341 (6153), 1238932. doi:10.1126/science.1238932.

Bishop, J.L., Schiffman, P., Southard, R., 2002. Geochemical and mineralogical analyses of palagonitic tuffs and altered rinds of pillow basalts in Iceland and applications to Mars. Geol. Soc. Lond. Spec. Publ. 202, 371–392.

Brand, B.D., White, C.M., 2007. Origin and stratigraphy of phreatomagmatic deposits at the pleistocene sinker butte volcano, western snake river plain, Idaho. J. Volc. Geotherm. Res. 160, 319–339.

Brand, B.D., Clarke, A.B., Semken, S., 2009. Eruptive conditions and depositional processes of Narbona Pass maar volcano, Navajo volcanic field, Navajo Nation, New Mexico (USA). Bull. Volcanol. 71, 49–77.

Brož, P., Hauber, E., 2013. Hydrovolcanic tuff rings and cones as indicators for phreatomagmatic explosive eruptions on Mars. J. Geophys. Res. Planets 118, 1656–1675.

Chang, C.-I., 2000. An information theoretic-based approach to spectral variability, similarity and discriminability for hyperspectral image analysis. IEEE Trans. Inf. Theory 46, 1927–1932.

Cloutis, E.A., Asher, P.M., Mertzman, S.A., 2002. Spectral reflectance properties of zeolites and remote sensing implications. J. Geophys. Res. 107, 5067. doi:10.1029/2000JE001467.

Cloutis, E.A., Gaffey, M.J., Smith, D.G., Lambert, R.S.J., 1990. Reflectance spectra of glass-bearing mafic silicate mixtures and spectral deconvolution procedures. Icarus 86 (2), 383–401.

Creighton, D.N., 1987. *Menan Buttes,* Southeastern Idaho. Geological Society of America Centennial Field Guide- Rocky Mountain Section, pp. 109–111.

Crisp, J., Kahle, A.B., Abbott, E.A., 1990. Thermal infrared spectral character of Hawaiian basaltic glasses. J. Geophys. Res. 95, 21657–21669.

Crumpler, L.S., Aubele, J.C., 2001. Volcanoes of New Mexico: an abbreviated guide for non-specialists. Volcanol. N. M.: N. M. Mus. Nat. Hist. Sci. Bull. 18, 5–15.

Degrave, E., Vanalboom, A., 1991. Evaluation of ferrous and ferric Mössbauer fractions. Phys. Chem. Miner. 18, 337–342.

Downs, R.T.the MSL Science Team, 2015. Determining mineralogy on Mars with the CheMin X-ray diffractometer. Elements 11, 45–50. doi:10.2113/gselements.11.1.45.

Drief, A., Schiffman, P., 2004. Very low temperature alteration of sideromelane in hyaloclastites and hyalotuffs from the Kilauea and Mauna Kea volcanoes: implications for the mechanism of palagonite formation. Clays Clay Miner. 52, 623–635.

Evans, D.L., Adams, J.B., 1980. Amorphous gels as possible analogs to martian weathering products. In: Proceedings of the 11th Lunar and Planetary Science Conference, pp. 757–763.

Farrand, W.H., Singer, R.B., 1991. Spectral analysis and mapping of palagonite tuffs of Pavant Butte, Millard County, Utah. Geophys. Res. Lett. 18, 2237–2240.

Farrand, W.H., Singer, R.B., 1992. Alteration of hydrovolcanic basaltic ash: observations with visible and near-infrared spectrometry. J. Geophys. Res. 97, 17393–17408.
Farrand, W.H., Lane, M.D., 2002. Spectral differences between palagonite tuffs formed in sub-glacial versus liquid water environments: relevance to Mars. In: Proceedings of the Lunar and Planetary Science XXXIII #1804.
Farrand, W.H., Lane, M.D., Edwards, B.R., 2008. North and south: Possible tuyas and hyaloclastite hills on the northern plains and in the southern Dorsa Argentea region of Mars. In: Proceedings of the Lunar and Planetary Science XXXIX #1761.
Farrand, W.H., Wright, S.P., Rogers, A.D., Glotch, T.D., 2016. Basaltic glass formed from hydrovolcanism and impact processes: characterization and clues for detection of mode of origin from VNIR through MWIR reflectance and emission spectroscopy. Icarus 275, 16–28.
Fisher, R.V., Schmincke, H.U., 1984. Pyroclastic Rocks. Springer-Verlag, Berlin, p. 472.
Godchaux, M.M., Bonnichsen, B., Jenks, M.D., 1992. Types of phreatomagmatic volcanoes in the western Snake River Plain, Idaho, USA. J. Volcanol. Geotherm. Res. 52, 1–25.
Hamilton, V.E., Morris, R.V., Gruener, J.E., Mertzman, S.A., 2008. Visible, near-infrared, and middle infrared spectroscopy of altered basaltic tephras: spectral signatures of phyllosilicates, sulfates, and other aqueous alteration products with application to the mineralogy of the Columbia Hills of Gusev Crater, Mars. J. Geophys. Res. 113, E12S43. doi:10.1029/2007JE003049.
Hammond, P., 1987. *Lone Butte and Crazy Hills: Subglacial Volcanic Complexes, Cascade Range, Washington*. GSA, pp. 339–344. Centennial Field Guide- Cordilleran Section.
Head III, J.W., Wilson, L., 2007. Heat transfer in volcano-ice interactions on Mars: synthesis of environments and implications for processes and landforms. Ann. Glaciol. 45, 1–13.
Horgan, B., Bell III, J.F., 2012. Widespread weathered glass on the surface of Mars. Geology 40, 391–394. doi:10.1130/G32755.1.
Horgan, B.H., Cloutis, E.A., Mann, P., Bell III, J.F., 2014. Near-infrared spectra of ferrous mineral mixtures and methods for their identification in planetary surface spectra. Icarus 234, 132–154.
Jakobsson, S.P., Moore, J.G., 1986. Hydrothermal minerals and alteration rates at Surtsey Volcano, Iceland. Geol. Soc. Am. Bull. 97, 648–659.
Jakobsson, S.P., Gudmundsson, M.T., 2008. Subglacial and intraglacial volcanic formations in Iceland. Jökull 58, 179–196.
James, F., 2004. *MINUIT Tutorial,* Function Minimization. CERN Computing and Data Processing School, Pertisau, pp. 10–24.
Jeong, G.Y., Sohn, Y.K., 2011. Microtextures, microchemistry, and mineralogy of basaltic glass alteration, Jeju Island, Korea, with implications for elemental behavior. Am. Mineral. 96, 1129–1147.
Klingelhöfer, G., Fegley Jr., B., Morris, R.V., Kankeleit, E., Held, P., Evlanov, E.N., Prilutski, O.F., 1996. Mineralogical analysis of Martian soil and rock by a miniaturized backscattering Mössbauer spectrometer. Planet. Space Sci. 44, 1277–1288.
Klingelhöfer, G., et al., 2003. Athena MIMOS II Mössbauer spectrometer investigation. J. Geophys. Res. 108, 8067. doi:10.1029/2003JE002138.
Korablev, O., et al., 2014. AOTF near-IR spectrometers for study of Lunar and Martian surface composition. In: Proceedings of the EPSC Abstracts, 9 EPSC2014-371-2.
Kruse, F.A., Lefkoff, A.B., Boardman, J.W., Heidebrecht, K.B., Shapiro, A.T., Barloon, P.J., Goetz, A.F.H., 1993. The spectral image processing system (SIPS) – interactive visualization and analysis of imaging spectrometer data. Remote Sens. Environ. 44, 145–164.
Leroi, V., Bibring, J.P., Berthe, M., 2009. Micromega/IR: design and status of a near-infrared spectral microscope for in situ analysis of Mars samples. Planet. Space Sci. 57, 1068–1075.
McIntosh, W.C., Chamberlin, R.M., 1994. 40Ar/39Ar geochronology of basaltic rocks and constraints on late cenozoic stratigraphy and landscape development in the red hill quemado area. In: Proceedings of the 45th Field Conference on New Mexico Geological Society Guidebook, 45. New Mexico, pp. 165–185.
Michalski, J.R., Kraft, M.D., Sharp, T.G., Williams, L.B., Christensen, P.R., 2006. Emission spectroscopy of clay minerals and evidence for poorly crystalline aluminosilicates on Mars from thermal emission spectrometer data. J. Geophys. Res. Planets 111, E03004. doi:10.1029/2005JE002438.
Morris, R.V., Gooding, J.L., Lauer Jr., H.V., Singer, R.B., 1990. Origins of Marslike spectral and magnetic properties of a Hawaiian palagonitic soil. J. Geophys. Res. 95 (B9), 14427–14434.
Morris, R.V., Golden, D.C., Bell III, J.F., Lauer Jr., H.V., Adams, J.B., 1993. Pigmenting agents in Martian soils: inferences from spectral, Mossbauer, and magnetic properties of nanophase and other iron oxides in Hawaiian palagonitic soil PN-9. Geochim. Cosmochim. Acta 57, 4597–4609.
Morris, R.V., et al., 2000. Mineralogy, composition, and alteration of Mars Pathfinder rocks and soils: Evidence from multispectral, elemental, and magnetic data on terrestrial analogue, SNC meteorite, and Pathfinder samples. J. Geophys. Res. 105, 1757–1817. doi:10.1029/1999JE001059.
Morris, R.V., Golden, D.C., Ming, D.W., Shelfer, T.D., Jorgensen, L.C., Bell III, J.F., Graff, T.G., Mertzman, S.A., 2001. Phyllosilicate-poor palagonitic dust from Mauna Kea Volcano (Hawaii): a mineralogical analogue for magnetic Martian dust? J. Geophys. Res. 106, 5057–5083. doi:10.1029/2000JE001328.
Morris, R.V., Klingelhöfer, G., Schröder, C., Fleischer, I., Ming, D.W., Yen, A.S., Gellert, R., Arvidson, R.E., Rodionov, D.S., Crumpler, L.S., Clark, B.C., Cohen, B.A., McCoy, T.J., Mittlefehldt, D.W., Schmidt, M.E., de Souza Jr, P.A., Squyres, S.W., 2008. Iron mineralogy and aqueous alteration from Husband Hill through Home Plate at Gusev Crater, Mars: results from the Mössbauer instrument on the spirit mars exploration rover. J. Geophys. Res. 113, E12S42. doi:10.1029/2008JE003201.
Oviatt, C.G., Nash, W.P., 1989. Late Pleistocene basaltic ash and volcanic eruptions in the Bonneville basin, Utah. Geological Society of America Bulletin 101 (2), 292–303.
Pauly, B.D., Schiffman, P., Zierenberg, R.A., Clague, D.A., 2011. Environmental and chemical controls on palagonitization. Geochem. Geophys. Geosyst. 12, Q12017. doi:10.1029/2011GC003639.
Pieters, C.M., 1983. Strength of mineral absorption features in the transmitted component of near-infrared reflected light: first results from RELAB. J. Geophys. Res. Solid Earth 88, 9534–9544.
Pieters, C.M., Mustard, J.F., Sunshine, J.M., 1996. Quantitative mineral analyses of planetary surfaces using reflectance spectroscopy. In: Dyar, M.D., McCammon, C., Schaefer, M.W. (Eds.). In: Mineral Spectroscopy: A Tribute to Roger G. Burns, 5. Geochemical Society, Houston, TX, pp. 307–325.
Ramsey, M.S., Christensen, P.R., 1998. Mineral abundance determination: quantitative deconvolution of thermal emission spectra. J. Geophys. Res. 103, 577–596.
Rogers, A.D., Aharonson, O., 2008. Mineralogical composition of sands in Meridiani Planum from MER data and comparison to orbital measurements. J. Geophys. Res. Planets 113, E06S14. doi:10.1029/2007JE002995.
Ruff, S.W., Christensen, P.R., Barbera, P.W., Anderson, D.L., 1997. Quantitative thermal emission spectroscopy of minerals: a laboratory technique for measurement and calibration. J. Geophys. Res. 102, 14899–14913.
Ruff, S.W., Christensen, P.R., Blaney, D.L., Farrand, W.H., Johnson, J.R., Michalski, J.R., Moersch, J.E., Wright, S.P., Squyres, S.W., 2006. The rocks of Gusev Crater as viewed by the Mini-TES instrument. J. Geophys. Res. 111, E12S18. doi:10.1029/2006JE002747.
Ruff, S.W., Christensen, P.R., Glotch, T.D., Blaney, D.L., Moersch, J.E., Wyatt, M.B., 2008. The mineralogy of Gusev crater and Meridiani Planum derived from the miniature thermal emission spectrometers on the spirit and opportunity rovers. In: Bell, III, J.F. (Ed.), The Martian Surface: Composition, Mineralogy, and Physical Properties. Cambridge University Press, New York, pp. 315–338.
Schiffman, P., Spero, H.J., Southard, R.J., Swanson, D.A., 2000. Controls on palagonitization versus pedogenic weathering of basaltic tephra: evidence from the consolidation and geochemistry of the Keanakako'I Ash Member, Kilauea Volcano. Geochem., Geophys., Geosyst. 1, 2000GC000068.
Schiffman, P., Southard, R.J., Eberl, D.D., Bishop, J.L., 2002. Distinguishing palagonitized from pedogenically-altered basaltic Hawaiian tephra: mineralogical and geochemical criteria. In: Smellie, J.L., Chapman, M.G. (Eds.). In: Volcano-Ice Interaction on Earth and Mars, 202. Geol. Soc. London, pp. 393–405. Spec. Publ..
Schopka, H.H., Gudmundsson, M.T., Tuffen, H., 2006. The formation of Helgafell, southwest Iceland, a monogenetic subglacial hyaloclastite ridge: sedimentology, hydrology and volcano-ice interaction. J. Volc. Geotherm. Res. 152, 359–377.
Smellie, J.L., Edwards, B.R., 2016. *Glaciovolcanism* on Earth and Mars: Products, Processes and Paleoenvironmental Significance. Cambridge University Press, p. 483.
Stroncik, N.A., Schmincke, H.U., 2001. Evolution of palagonite: crystallization, chemical changes, and element budget. Geochem. Geophys. Geosyst. 2. doi:10.1029/2000GC000102.
Stroncik, N.A., Schmincke, H.-U., 2002. Palagonite – a review. Int. J. Earth Sci. 91, 680–697.
Vandenberghe, R.E., De Grave, E., de Bakker, P.M.A., 1994. On the methodology of the analysis of Mössbauer spectra. Hyperfine Interact 83, 29–49. doi:10.1007/BF02074257.
Walton, A.W., Schiffman, P., 2003. Alteration of hyaloclastites in the HSDP 2 Phase 1 Drill Core: 1. Description and paragenesis. Geochem. Geophys. Geosyst. 4 (5), 8709. doi:10.1029/2002GC000368.
White, J.D.L., 1996. Pre-emergent construction of a lacustrine basaltic volcano, Pahvant Butte, Utah (USA). Bull. Volcanol. 58, 249–262.
Wiens, R.C., et al., 2016. The SuperCam Remote Sensing Instrument Suite for Mars 2020, 47th Lunar and Planetary Science Conference abstract #1322.
Wohletz, K.H., Sheridan, M.F., 1983. Hydrovolcanic explosions II. Evolution of basaltic tuff rings and tuff cones. Am. J. Sci. 283, 385–413.
Womer, M.B., 1977. The origin of split butte: a maar type crater of the south-central snake river plain, Idaho. In: Greeley, R., King, J.S. (Eds.), Volcanism of the Eastern Snake River Plain, Idaho: A Comparative Planetary Geology Guidebook. NASA, pp. 189–202. CR-154621.